Mironov, Camelia M., Ph.D., October, 2005 NUCLEAR PHYSICS

CHARGED KAON PRODUCTION IN P+P AND D+AU COLLISIONS,

THE BASELINE COMPARISON SYSTEMS FOR UNDERSTANDING

AU+AU COLLISIONS AT RHIC (104 pp.)

Director of Dissertation: Spyridon Margetis

One of the primary challenges in modern nuclear physics is to understand the properties of hot nuclear matter. The expectation is that at sufficiently high energy densities, nuclear matter undergoes a phase transition where individual nucleons 'dissolve' and a plasma of freely moving quarks and gluons is formed. To accomplish this in the laboratory, normal nuclear matter is heated and compressed through collisions of heavy nuclei at relativistic energies.

The Relativistic Heavy Ion Collider (RHIC) at Brookhaven National Laboratory is a dedicated particle accelerator, capable of colliding nuclear beams to energies up to $100\,\mathrm{GeV}$ per nucleon per beam. Particle species ranging from protons ($A{=}1$) to gold ($A{=}197$) are accelerated in this state-of-the-art facility and collide at selected intersection points.

In this dissertation, a detailed transverse momentum (p_T) analysis is made at central rapidities, using the STAR Time Projection Chamber (TPC). The data set is comprised of about 10 million d+Au and about 6 million p+p events at $200\,\mathrm{GeV}$. Previously analyzed data from a 2002 Au+Au run are also used. This work concentrates on the study of identified charged kaons (K^+, K^-), which are the lightest strange mesons and hence the particles that dominate strangeness production.

Charged kaons are identified using a topological reconstruction method which has relatively large p_T coverage.

In this dissertation, we present p_T and yield systematics. We find that the particle to anti-particle ratio is p_T independent in all colliding systems studied, an indication that in the p_T range studied, the pQCD regime is not reached yet. The ratios, close to unity, signal a rather net-baryon-free mid-rapidity region. The $\langle p_T \rangle$ in central d+Au collisions is larger than in peripheral Au+Au collisions, which might hint at the presence of 'Cronin effect' in the dAu system as explained.

We also obtain results on nuclear modification factors (R_{CP}^{dA} - central to peripheral ratio, R_{dA}, R_{AA} - geometrically scaled Au+Au(d+Au) to p+p ratios) which are presented for various mesons and baryons. In d+Au collisions, an enhancement compared to binary scaling of both R_{CP}^{dA} and R_{dA} is observed, an experimental observation called 'Cronin effect'. This result is thought to be an initial-state effect. In contrast, the same ratio in central Au+Au collisions exhibits a suppression instead of an enhancement. This was understood in terms of a dense partonic medium which induces energy loss via gluon radiation by a high-energy parton traversing the medium, and leads, after fragmentation, to hadrons with lower $\langle p_T \rangle$. The meson-baryon differences, first observed in Au+Au R_{CP}^{AA}, also exist in d+Au collisions.

CHARGED KAON PRODUCTION IN P+P AND D+AU COLLISIONS,
THE BASELINE COMPARISON SYSTEMS FOR UNDERSTANDING
AU+AU COLLISIONS AT RHIC

A dissertation submitted to
Kent State University in partial
fulfillment of the requirements for the
degree of Doctor of Philosophy

by

Camelia M. Mironov

October, 2005

Dissertation written by

Camelia M. Mironov

B.S., University of Bucharest (Romania), 2001

Ph.D., Kent State University (USA), 2005

Approved by

—————————————————— , Chair, Doctoral Dissertation Committee

—————————————————— , Members, Doctoral Dissertation Committee

—————————————————— ,

—————————————————— ,

—————————————————— ,

Accepted by

—————————————————— , Chair, Department of Physics

—————————————————— , Dean, College of Arts and Sciences

Table of Contents

List of Figures

List of Tables

Acknowledgments

Multumesc Mama, Tata, Misu! Voua va datorez mare parte din ceea ce sunt eu astazi. To them, my family, I owe most of what I am today.

The rest is the result of a lucky encountering with extraordinary people: Carmen and Makis who cared and made everything possible, Lee who adopted me and guarded me on the science road (an endless job it seems), Gene who let me transform him in my personal science/computing oracle (an annoying job most of the time, but gracefully managed), Helen a one-woman/scientist-show who forced me face reality and gave me strength to continue and fight, Ben for patience and help, Professor Margetis (Spiros) who trusted me and gave me wings to fly.

I will never forget where I've started from and how I got here.

Chapter 1

Heavy Ion Collisions and Quark Gluon Plasma

1.1 Introduction
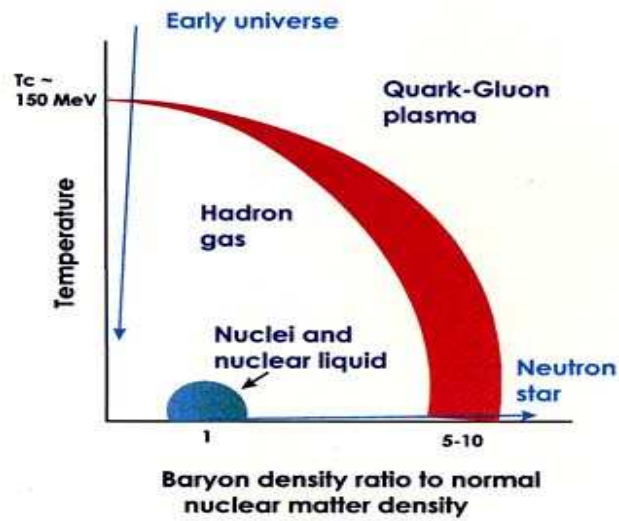
Figure 1.1: Schematic phase-diagram of nuclear matter.

Generally speaking, by 'plasma' one understands a quasi-neutral, charge-separated system (number of positive and negative charges are approximately the same), with weakly interacting components which exhibits collective effects. By extrapolation, Quark-Gluon Plasma (QGP) would be a quasi-neutral, deconfined system of quarks, anti-quarks (the building blocks of matter according to Quantum Chromo Dynamics, QCD) and gluons (the strong interaction force carriers), with weak mutual color interactions which act collectively [1].

In Figure 1.1 a schematic version of a phase-diagram of nuclear matter is presented. Regions of temperature and baryon density in which matter exists as a nuclear liquid,
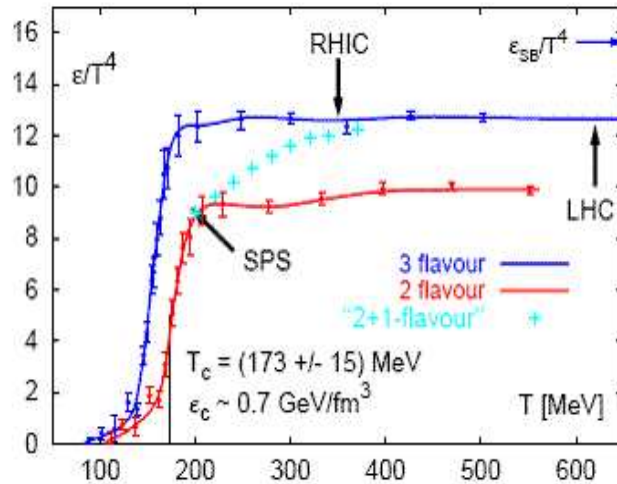
Figure 1.2: The energy density in QCD with 2 and 3 light quarks and also the calculation for the case where the strange quark mass is fixed to $m_s \sim T_C$.

hadron gas or quark-gluon plasma are shown. The path followed by the early universe as it cooled from the QGP phase to normal nuclear matter is shown as the left arrow while the bottom arrow traces the path taken by neutron stars as they form. Heavy-ion collisions follow a path between these two extremes, an increase of temperature and/or baryon density being possible. We produce such collisions in laboratory in an attempt of reproducing the QGP formation conditions, creating it, recognizing its presence and describing its properties.

The existence of a QGP can be theoretically inferred through QCD calculations on a lattice [2]. These calculations predict a phase transition from confined hadronic matter (such as protons and neutrons) to a de-confined state in which hadrons are dissolved into quarks and gluons (or *partons*) at a temperature $T_C \sim 170\,\mathrm{MeV}$ which corresponds to an energy density $\epsilon \simeq 0.7\,\mathrm{GeV/fm^3}$, nearly an order of magnitude larger than cold nuclear matter. In Figure 1.2, the black arrows indicate the temperatures reached in the initial stage of heavy-ion reactions at SPS, RHIC and at LHC (a
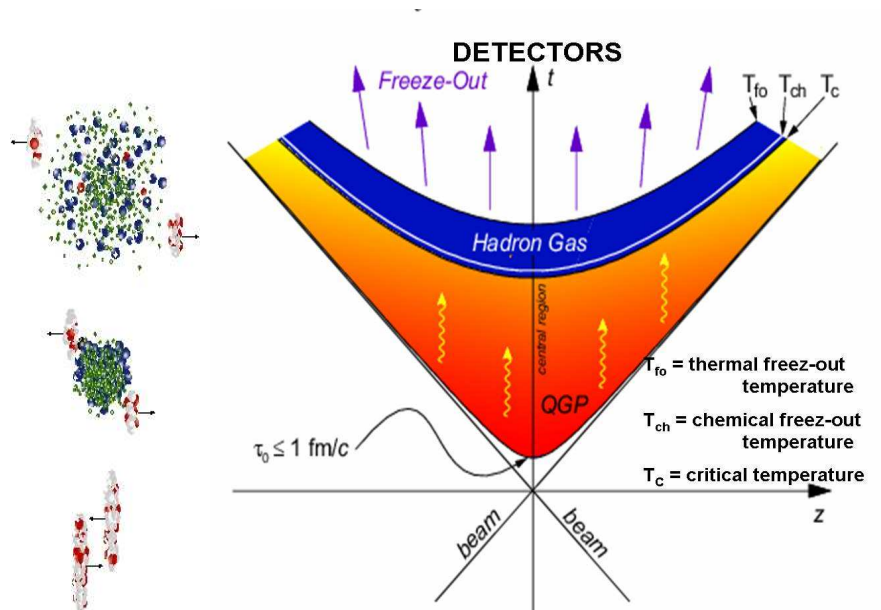
Figure 1.3: The space-time picture and the different evolution stages of a relativistic heavy-ion collision.

future accelerator under construction at the CERN laboratory). The colored arrow indicates the Stefan-Boltzmann limit for an ideal gas. The transition can be understood in terms of number of degrees of freedom [3]. Above T_C, the gluon [8(color) $\times$ 2(spin) for a total of 16] and quark [2-3(light flavors) $\times$ 2(quark-antiquark) $\times$ 3(colors) $\times$ 2(spin) for a total of 24-36] degrees of freedom are activated. In the quark-gluon plasma, there are then about 40-50 internal degrees of freedom in the temperature range $(1-3)\,T_C$, while at low temperature, the pion gas has 3 (π^+, π^-, π^0). Since the energy density is roughly proportional to the number of degrees of freedom, one understands this rapid change in the energy density in a narrow temperature window as a change in the number of degrees of freedom between confined and deconfined matter.

Nucleus-nucleus collisions are a process to heat and/or compress atomic nuclei. The variation of the collision energy and the system size allows us to control the degree to

which this happens. Figure 1.3 depicts the schematic space-time evolution of heavy-ion collisions. In the early stages of a collision, a QGP is created if the temperature of the system exceeds T_C, the critical temperature at which the transition to partonic degrees of freedom occurs. After creation of partonic matter, the system expands, cools and drops below T_C, after which it passes through chemical freeze-out temperature T_{ch}, when the inelastic scattering stops and the relative abundances of particle types stabilizes. The system cools further until the kinetic freeze-out occurs at temperature T_{fo} below which the elastic collisions also end. After this, the particles free-stream into the detectors without further interactions.

1.2   RHIC and QGP

Essentially, the question 'Is Quark-Gluon Plasma created at RHIC?' has three aspects: are the formation conditions present (high energy density and/or temperature), what are the necessary and sufficient observation to confirm the presence of the QGP and how to probe the properties of the plasma?

For identifying the formation of the plasma and studying its properties, different probes and several tools were proposed in order to overcome several impediments: the expected very small size (a few fermi), the very short life time ($< 1\,\mathrm{fm/c}$) of the state, and the huge background. An example of this background is the thermal photon emission from the hadronic π^0 decays which overlap the prompt photon emission of the plasma. The signals are also expected to be modified by the final state interactions in the hadronic phase [4]. Flow [5] (to probe the collective motion), quarkonium suppression [6] and strangeness enhancement [7] (to probe deconfinement), photons, lepton pairs [8] (to probe the initial stages) and high p_T hadrons (for probing the density of the created medium), are all among the signatures proposed over the years

to identify a QGP. A less demanding approach was taken recently [9], in which there are just three necessary ingredients for claiming a QGP, the rest being just tools for finding and describing the properties of the plasma. In this view, a) a class of observables is needed to provide information about bulk collectivity (flow measurements are considered to be the key), b) another class is required to probe the color density of the medium (high p_T partons) and finally, c) there is a need for a control experiment to differentiate between the competing nuclear effects (initial vs. final state effects) as well as the production mechanisms. Though these measurements and observables are for sure *necessary* for claiming QGP creation, debates are still ongoing regarding whether they can be considered as *sufficient* proof of QGP formation. Having this remark in mind, we present in the following some broad features of the matter created at RHIC.

1.2.1   Energy density

A pre-requisite for creating QGP is to produce a system with sufficiently large energy density (ϵ). Before any calculations, we first want to make a note on the amount of available energy in a collision between two relativistic Au ions at RHIC. Each gold ion is accelerated to a center of mass energy of 100 GeV per nucleon, hence the total energy carried by each nucleus is 100×197 GeV (or 19.7 TeV). The average energy loss of the colliding nuclei is ~ 73 GeV/nucleon [10] which means that as much as 197×73 GeV ($\sim$29 TeV) of kinetic energy is removed from the beams per Au+Au central collisions and is available for particle production in a small volume[1] immediately after the collision. Compared to the temperature in the center of the

---

[1]~ 20 fm^3, if we consider the volume $V \simeq \Delta t \times \pi R^2 \times 2R/\gamma$ created in a time $\Delta t \simeq 1$ fm/c of a collision of two Au ions of radius $R \simeq 7$ fm, Lorentz contracted with $\gamma = E/(m_0 c^2) = 100(GeV)/.938(GeV/c^2)c^2 \simeq 106$.

Sun, 15,000,000,000 ^{o}K, this means that a temperature $\sim$20 000 times bigger can be achieved in central Au-Au collisions, using the Boltzmann constant $k_B = 8.6 \times 10^{-5}$ eV K^{-1} and energy $E \sim k_B T$, where T is the temperature.

There are several ways of estimating the energy density of the system created. A traditional one is using the Björken formula [11] Eq. 1.1, derived from relativistic hydrodynamic considerations. In this approach, the energy density of the system is estimated in terms of the transverse energy rapidity[2] density $dE_T(\tau_{form})/dy$ (assuming it is independent of rapidity around $y = 0$), the transverse system radius, R (assuming a thin disk for each incoming colliding nucleus) and a formation time τ_{form}, when all the particles are formed, and after which they all move hydrodynamically.

$$(1.1) \qquad \epsilon_{BJ} = \frac{1}{\tau_{form}} \frac{1}{\pi R^2} \frac{dE_T(\tau_{form})}{dy}$$

Assuming a formation time $\tau_{form} = 1$ fm/c and using the STAR value for the measured value of the transverse energy per unit rapidity, $\sim$621 GeV [12], $\epsilon_{BJ} \sim 5$ GeV/fm^3. A few caveats have to be mentioned when quoting results obtained using the Björken formula. First of all, there is no information in this formula related to the degree of thermalization[3] of the system. Also, as the system expands, it performs work ($p\Delta V$) and consequently $\epsilon_{real} > \epsilon_{BJ}$. Given all these, we notice that the result mentioned is actually a lower limit, because also the formation time used of 1 fm/c (used also for SPS energies) is expected to be shorter at RHIC. The PHENIX experiment performed a more realistic estimate [13] and obtained $\tau_{form} \sim 0.35$ fm/c, which would mean $\epsilon_{BJ} \sim 14$ GeV/fm^3.

---

[2]rapidity y of a particle is defined in terms of its energy-momentum components p_0 and p_z by $y = \frac{1}{2} \ln(\frac{p_0 + p_z}{p_0 - p_z})$

[3]the process by which particles reach thermal equilibrium through mutual interactions (i.e. the energy distribution of the system is of Maxwell-Boltzmann type)

Another way the energy density can be inferred is by estimating the energy loss that a high p_T parton[4] suffers while traversing the medium via gluon radiation, before fragmenting into hadrons. Since the parton energy loss (measured via the hadron fragments) is proportional to the gluon density of the medium, the gluon density can be calculated, and from that the energy density of the system can be estimated. Following this logic, $\epsilon \sim 15\,\mathrm{GeV/fm^3}$ [14].

Another number for the energy density reached in central Au+Au collisions at RHIC is the one used in hydrodynamic models. There, assuming a thermalized medium, it is necessary to set the initial energy density to $\epsilon = 25\,\mathrm{GeV/fm^3}$ at $\tau_{form} = 0.6\,\mathrm{fm/c}$ in the fireball center, in order to describe the spectra and flow measured at RHIC [15]. Although all these calculations give different results, what we want to stress is that all numbers are significantly in excess ($\sim$7-35 times) of the value $\sim 0.7\,\mathrm{GeV/fm^3}$ predicted by lattice QCD for the transition to quark gluon plasma.

Now that we established that the initial energy densities achieved in RHIC collisions can be high enough to produce a quark-gluon plasma, we have to go further and ask about the probes which could provide unambiguous information on the state of matter produced during the collision. What observables are necessary and sufficient for concluding that QGP was discovered?

1.2.2   QGP signatures

Elliptic Flow

A way to probe the collective motion of the de-confined partons that exists in QGP is to measure the elliptic flow v_2 generated by the transformation of the initial anisotropy in coordinate space into a momentum space anisotropy through constituent

---

[4]generic name for quarks and gluons
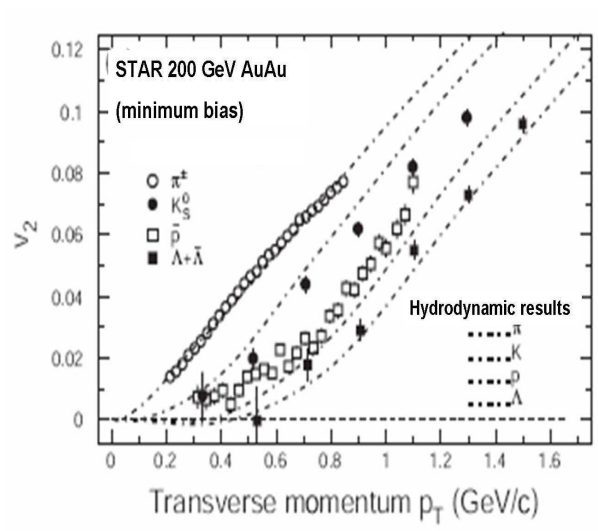
Figure 1.4: Azimuthal elliptic flow, $v_2(p_T)$, for different mesons and baryons in Au+Au at 200 GeV.

interactions [5] (for details on flow, see Appendix A). As the volume expands, the spatial anisotropy reduces, and the momentum anisotropy saturates. This makes the elliptic flow sensitive to the early collision stages.

At RHIC, hydrodynamic models can describe both spectra and $v_2(p_T)$ unlike at lower energies [18]. In Figure 1.4, the agreement between the hadron mass dependence of the elliptic flow in hydro models and the experimental data is striking. This shows that there is an azimuthally asymmetric flow velocity field.

High p_T probes

Hard-scattered partons suffer energy loss from gluon radiation [19]. The amount of the loss depends on the density of the medium the parton is traversing. The reduction in the parton energy translates to a reduction in the average momentum of the fragmentation hadrons, which in turn produces a suppression in the yield of high p_T hadrons relative to the corresponding yield in baseline p+p collisions. Thus the suppression of the yield of high p_T hadrons is believed to provide a direct experimental
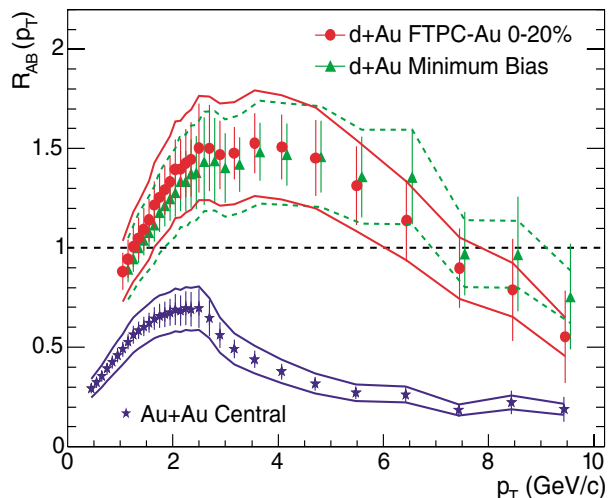
Figure 1.5: R_{dA} and R_{AA} plots for hadrons in STAR.

probe of the density of color charges in the medium through which the parton passes. In Figure 1.5, the ratio of the inclusive hadron yield in central Au+Au collisions (blue) to the geometrically-scaled yield from p+p collisions (R_{AB}) is presented. A strong suppression compared to scaled p+p data is present, suggesting that a dense medium is created, unlike at lower energies [29]. More than this, two-particle azimuthal correlations (for details see Appendix A) reveal that the correlation at $\Delta\phi = 2\pi$, expected from balancing jets created in the partonic hard-scattering is suppressed compared to p+p collisions. The back-to-back partner of the dijet disappears into the bulk matter generated in the collisions, one more proof for the opacity of the medium created in 200 GeV central heavy-ion collisions at RHIC (Figure 1.6).

Partonic final state energy loss

After the high p_T yield suppression and the disappearance of the back-to-back azimuthal jet correlation was observed in central Au+Au collision compared to baseline p+p collisions, there was a need for one last discriminant control experiment. There
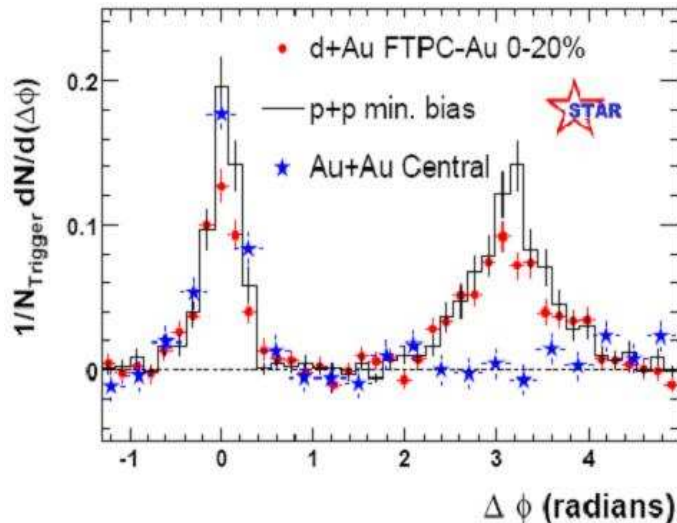
Figure 1.6: Dijet azimuthal correlations for hadrons in p+p, d+Au and Au+Au. The absence of quenching in the back peak in d+Au supports the conclusion that the suppression in R_{AA} is due to final state energy loss.

was need for an experiment to confirm that the observations in Au+Au are indeed due to the medium created during the collision and can not be explained by the initial state effects (e.g. multiple scattering, gluon saturation etc). The control experiment is d+Au, where all the initial state effects of Au+Au are present, but no final dense medium is formed[5]. The results, in red in Figures 1.5 and 1.6, no suppression of the high p_T yield and the reappearance of the back-side jet, confirm that the quenching in Au+Au is a final state effect.

We also want to mention another alternative explanation of the final state suppression that was ruled out by a theoretical calculation. Gallmeister and collaborators [30] investigated the possibility that the suppression is due to final state *hadronic* interactions of the formed hadrons with the bulk hadronic matter which would lower the energy and hence result in suppression. The calculation presented in Figure 1.7 in the

---

[5]by *initial* and *final* effects we are referring to *before* and *after* the hard collision of two partons took place
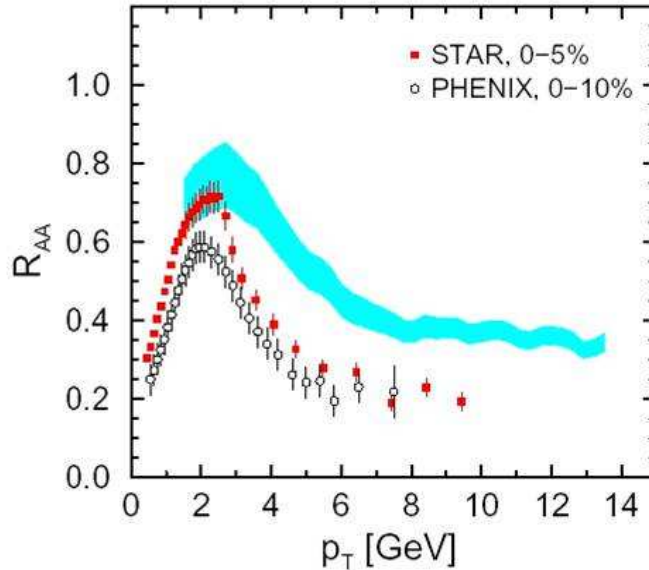
Figure 1.7: Comparison of theoretical calculations [30] with experimental R_{AA}. Hadronic final state energy loss (blue band) can not reproduce the entire suppression.

form of the colored blue band along with PHENIX and STAR data. The final state hadronic energy loss can not reproduce the factor of 5 suppression observed, one more proof that *partonic* energy loss is necessary to reproduce the observed suppression.

1.3   A p_T analysis of the collision products

1.3.1   pQCD for $p_T > 2.\text{GeV/c}$

High p_T hadron production in p+p collisions can be calculated within the perturbative QCD (pQCD) parton model [21]. Starting with two-body scattering at the parton level ($ab \rightarrow bc$), the expression for the production of hadrons h can be written as

$$(1.2) \qquad \frac{d\sigma_{pp}^h}{dyd^2p_T} = K \sum_{abcd} \int dx_a dx_b f_{a/N}(x_a, Q^2) f_{b/N}(x_b, Q^2) \frac{d\sigma^{ab \rightarrow cd}}{d\hat{t}} \frac{D_{h/c}^0(z_c, Q^2)}{\pi z_c}$$

where $f_{a/N}(x_a, Q^2)$ and $f_{b/N}(x_b, Q^2)$ are the parton distribution functions (PDF) of the parton a inside nucleon N 'observed' at a momentum scale Q^2, carrying the fraction
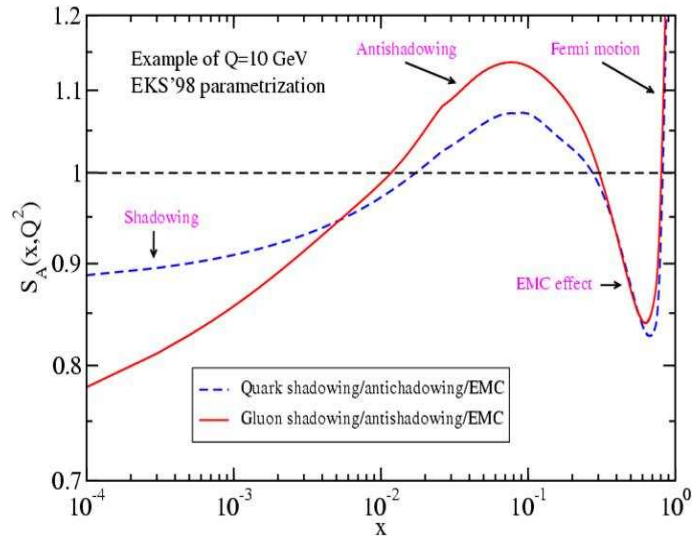
Figure 1.8: Nuclear modification effects, in EKS parametrization [28]. $S_{a/A}(x, Q^2) = f_{a/A}(x, Q^2)/f_{a/p}(x, Q^2)$ vs. $x = 2p_T/\sqrt{s}e^{-y}$. At mid-rapidity RHIC, $x < 10^{-3}$.

momentum x within the incoming hadron, $D^0_{h/c}(z_c, Q^2)$ is the fragmentation function

of parton c into hadron h (known from e^+e^- data), z_c is the momentum fraction of the

parton c carried by the hadron h and $d\sigma^{ab \to cd}/d\hat{t}$ is the hard-scattering cross-section.

The factor K is a phenomenological one, used to account for higher order QCD

corrections to the jet cross-section. This formalism describes p+p($\bar{p}$) data from $\sqrt{s} =$

0.2 ([24]) to 1.8 TeV ([25]) and because of this, constitutes a good starting point for

the study of p+A and A+A collisions. In these more complex cases though, additional

factors and phenomena, pertaining to both initial (before hard scattering) and final

state have to be considered. The PDF is modified in bound nucleons compared

to free nucleons: shadowing, anti-shadowing, and the EMC effect have to be taken

into account depending on the value of x (which for mid-rapidity RHIC collisions is

$< 10^{-3}$ Figure 1.8).In addition, multiple soft scattering of the projectile parton (or

nucleon) may boost its transverse momentum before it undergoes the hard-scattering.

Finally, the nuclear medium produced in the collision might influence the production

of high p_T hadrons via partonic or hadronic re-scattering with the medium created in the collision. Incorporating all these effects (pertaining to both initial and final state) into Equation 1.2 [26], the inclusive hadron results (both Au+Au central to peripheral and Au+Au central to p+p ratios) are well reproduced [27], therefore, it can be concluded at this point that pQCD is the right theory which describes the inclusive hadrons from p+p to A+A systems at RHIC, and the parton fragmentation is the mechanisms through which the high p_T hadrons are produced.

1.3.2 p+p, d+Au, Au+Au collisions

We are coming back now in more detail to the methods by which we compare the Au+Au results (influenced by both initial and final state effects) to the simpler systems, d+Au (initial state effects, but no final medium) and the baseline p+p collisions.

A simple way to study quantitatively the nuclear medium effects is by determining the **Nuclear modification factor** R_{AB}

$$(1.3) \qquad R^h_{AB} = \frac{1}{< N^{AB}_{binary} >} \frac{d^2 N^h_{AB}/dp_T/dy}{d^2 N^h_{pp}/dp_T/dy}$$

where $d^2 N^h/dp_T/dy$ is the hadron differential yield and $< N^{AB}_{binary} >$ is the mean number of binary nucleon-nucleon collisions. That $R_{AB} < 1$ for $p_T > 2\,\text{GeV/c}$ is considered a consequence of the partonic energy loss in the medium generated in the collision, while an experimental $R_{AB} > 1$ value is called Cronin effect[6], and is traditionally attributed to soft parton scattering prior to the hard collision[7].

---

[6]The name comes from the first paper reporting this enhancement in pA collisions, published by J.W.Cronin et al in 1975 [67]

[7]The *hardness* of the rescattering process taken into account can be understood in two ways. Commonly it is said about a parton that undergoes a 'hard' scattering if the exchange momentum is grater than approximately $1\,\text{GeV/c}$. However, since physically there is no sharp distinction between

Experimentally it is easier to measure the central (head-on collisions) to peripheral (big impact parameter) ratio, R_{CP} (Equation 1.4) instead of R_{AB}, because of the lack of statistics for p+p data and the fact that many of the measurement uncertainties cancel out when comparing central to peripheral data for the same colliding system.

$$(1.4) \qquad R_{CP}^h = \frac{d^2 N_{central}^h/dp_T/dy/}{d^2 N_{peripheral}^h/dp_T/dy} \frac{< N_{binary}^{central} >}{< N_{binary}^{peripheral} >}$$

The assumption made is that the peripheral Au+Au, d+Au and p+p data are similar, in the sense that in no dense medium is created in these systems. Accordingly, the results on unidentified charged hadron inclusive yield are similar: both ratios (R_{CP} and R_{AA}) were suppressed in Au+Au [31], and both enhanced in d+Au [32, 33]. The conclusion was that the suppression seen in central Au+Au is not an initial state effect, but rather a final state effect.

Models can describe the features seen in the charged hadron spectra by assuming initial-state soft-scattering in all collisions, plus jet quenching in Au+Au collisions and [31, 34]. A new challenge appeared when the Au+Au R_{CP} was measured for identified hadrons in the intermediate transverse momentum region between 2 and $6\,\mathrm{GeV/c}$ [35]: the kaons were showing a suppression starting around $1.5\,\mathrm{GeV/c}$, while the Λ hyperons started to be suppressed only above $2.5\,\mathrm{GeV/c}$, with both curves coming again together around $6\,\mathrm{GeV/c}$. The question which arose was whether the effect observed was purely a mass dependent effect, or an actual baryon-meson difference. A first answer, as proposed by coalescence models (see [37] and the references therein), was that the difference is species dependent: the baryons need three quarks

---

hard and soft momentum transfer, we can make reference to the two-component models of hadron spectra and call 'hard' a scattering which is descried by a power-law differential cross-section at large p_T, and 'soft' a scattering whose cross-section is decreasing faster than the inverse power of the transverse momentum at large p_T.

to coalesce while mesons require only two, and this pushes the baryon suppression to higher p_T. The experimental confirmation can be seen in the R_{CP} for other mesons and baryons: a clear separation between baryons and mesons above $1.5\,\mathrm{GeV/c}$ is visible, independent of the meson masses [36]. It is expected that the particle specific measurements of R_{AA} would confirm all the R_{CP} observations, similar to the results in non-identified particle studies.

1.4 Strangeness

There are basically two ideas behind the collective enhancement of strangeness production in a QGP phase compared to hadron gas (HG) phase. 1. The difference in the production mechanisms of strangeness in a QGP (individual strange quark pair production from a dense system of gluons and light quarks) and in a HG (hadrons with opposite strangeness from inelastic hadron-hadron interactions). 2.The equilibration timescale for producing strange particles is much smaller in a quark-gluon plasma than in a hadron gas, so that the produced strange particles are not suppressed by dynamical effects and the corresponding number density is close to the equilibrium value [38].

The first idea can be illustrated by making a short calculation of the energy threshold ($E_{threshold}$) for strangeness production in QGP and HG. The associated production of a $s\bar{s}$ quark pair can proceed by the fusion of two gluons or two light quarks ($q \equiv u, d$)

$$q + \bar{q} \to s + \bar{s} \qquad g + g \to s + \bar{s}$$

so that, in the case of QGP, the threshold is given by the rest mass of the strange-antistrange quark pair

$$E_{threshold}^{QGP} = 2m_S \approx 300 MeV.$$

where m_S is the strange quark mass.

On the other hand, hadronic strangeness production (most often via $\pi\pi \rightarrow K\overline{K}$, $\pi N \rightarrow K\Lambda$, $NN \rightarrow N\Lambda K$) proceeds in vacuum with considerably larger energy threshold

$$E^{HG}_{threshold} = 2m_K - 2m_\pi \approx 710 MeV \qquad E^{HG}_{threshold} = m_\Lambda + m_K - m_N \approx 670 MeV$$

$$E^{HG}_{threshold} = m_\Lambda + m_K - m_N - m_\pi \approx 530 MeV.$$

Furthermore, since multi-strange hadrons (e.g. Ω, Ξ) have to be created in multi-step reactions, as a strange particle has to be created first and then the multi-strange one, they are even more suppressed than single-strange hadrons in a HG compared to QGP. For the second idea, we will analyze the cross section production of an $s\bar{s}$
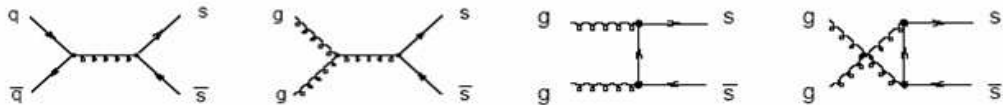
Figure 1.9: Feynman diagrams for the production of strange and anti-strange quarks in a quark-gluon plasma.

pair using the Feynman diagrams in Fig. 1.9, in first order perturbation theory. For the cross-section involving quarks [39]

$$(1.5) \qquad \sigma_{q\bar{q} \rightarrow s\bar{s}} = \frac{8\pi\alpha_s^2}{27s}(1 + \frac{2m_s^2}{s})(1 - \frac{4m_s^2}{s})^{1/2} = \frac{8\pi\alpha_s^2}{27s^2}(s + 2m_s^2)\chi$$

with $\sqrt{s}$ the total center of mass energy and $\chi = \sqrt{1 - 4m_s^2/s}$.

The cross section has a threshold at $\sqrt{s_{NN}}=2m_S$, rises steeply, reaches a maximum and falls rapidly (Fig. 1.10). The strange-antistrange quark pair production via gluon fusion dominates over the quark production cross section for higher energies, so not only is strangeness production energetically favorable in QGP, but the
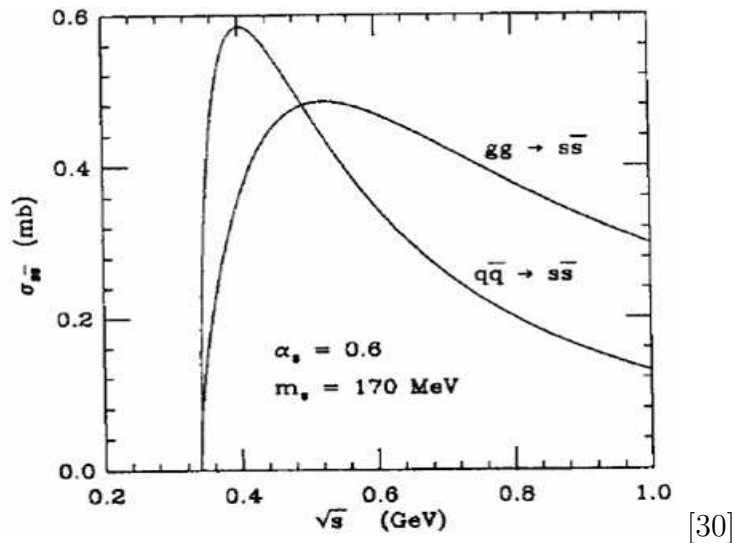
Figure 1.10: The averaged strangeness production cross-section as a function of colliding energy.

creation probability is larger. Because gluons are very efficient in generating strange anti-strange quark pairs in gluon plasma, the transient presence of gluons may be inferred from the appearance of anomalously high strange particle abundance which practically saturates the available strange quark phase. In addition, the mass of the strange quarks and anti-quarks $(m_S(2\,GeV) \sim 100\,MeV)$ is of the same magnitude as the temperature at which the hadrons (protons,neutrons etc) are expected to melt into quarks. This means that the abundance of strange quarks is sensitive to the conditions, structure and dynamics of the deconfined-matter phase. Since the strange quarks are not brought in the reaction by the colliding nuclei (like the light quarks, u and d, thorough the constituent protons and neutrons of the colliding nuclei), we have the guarantee that any strangeness that we detect, is made from the kinetic energy of the colliding nuclei.

The basic process for strange quark production (the pair production process, $gg \to s\bar{s}$) is, in principle the same for both phases of hadronic matter, hadron gas and quark

gluon plasma. However, in the HG case of well separated individual hadrons with the non-perturbative QCD vacuum in between, the mentioned reaction can only take place during the actual collision process of two individual hadrons. This means that strange quark production experiences severe constraints in space and time [40]. Also, because all the initial and final state hadrons are color singlets, the effective number of the available degrees of freedom is greatly reduced in comparison to the quark-gluon plasma phase.

Strange hadrons are easy to detect via the tracks left by their decay products, the decay weak interaction occurring in general, on a time scale much longer than the nuclear-collision times ($\sim 10^{23}$ s). The topological reconstruction of strange hadrons permits the measurement of identified spectra over a large p_T range, making possible the study of baryon-meson and particle-antiparticle differences, parton-flavor and mass dependencies. Strange hadrons allow the characterization of the medium in a more detailed and specific way, which goes beyond the unidentified hadron measurements.

The Experiment

2.1   The Machine
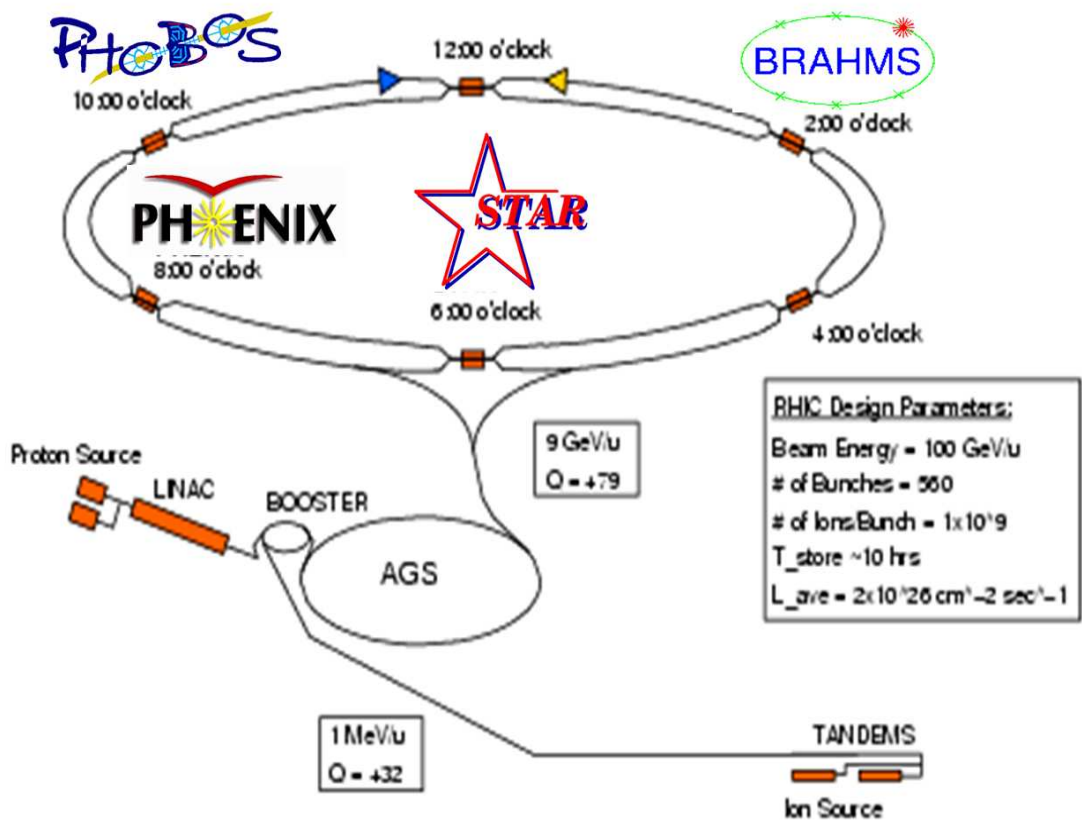
Figure 2.1: RHIC facility at Brookhaven National Laboratory

The construction of the Relativistic Heavy Ion Collider (RHIC) (Figure 2.1) and the complementary set of four detectors (STAR, PHENIX, BRAHMS, PHOBOS) had as a primary objective to investigate the formation and the properties of the quark

Year	System	$\sqrt{s_{NN}}$
2000	Au+Au	56 (one day), 130
2001	Au+Au, p+p	200
	Au+Au	20 (one day)
2003	d+Au, p+p	200
2004	Au+Au, p+p	200
	Au+Au	63
2005	Cu+Cu, p+p	200
	Cu+Cu	62, 22

Table 2.1: History of RHIC Runs, 2000 - 2005

gluon plasma (QGP) phase [41]. RHIC also is the first machine in the world capable of colliding polarized protons beams, making possible experiments that are important for studying the spin structure of nucleons.

Having two completely independent superconducting rings and using as a particle sources two tandems Van de Graaf and a proton linac, the facility permits the study of both symmetrical (e.g. gold-gold, copper-copper, proton-proton) and asymmetrical colliding systems (such as deuteron-gold). The particles that can be accelerated, stored and collided range from A=1 (protons) to $A \simeq 200$ (gold). The top energy for heavy ion beams is $100\,\mathrm{GeV}$/nucleon and for protons is $250\,\mathrm{GeV}$. In order to understand the properties of the nuclear matter obtained in central gold-gold collisions, systems of smaller size and lower energy were also studied; we present in Table 2.1 a history of all these RHIC runs, starting with the first day (June 12, 2000) until the present (2005).

2.2   The Collider Facility

Colliding ions in RHIC is a multi-step process [42]. Negatively charged ions (A^{-1} or d^{-1} for example) from a pulsed sputter ion source are partially stripped of their electrons and then accelerated in the Tandem van de Graaff. After further stripping

(for gold ions this corresponds to a charge state of +32) at the exit of the Tandem, the ions are delivered to the Booster Synchrotron where they are accelerated more. The ions are stripped again at the exit of the Booster (e.g. gold ions reach a +77 charge state at this stage) and injected to the AGS for acceleration to the RHIC injection energy. Fully stripped state (+79 for gold ions) is reached at the exit of the AGS. In p+p collisions, the protons are injected into the Booster synchrotron directly from the LINAC (LINear ACcelerator), accelerated in the AGS and finally injected in the RHIC. The Collider itself consists of two concentric accelerator/storage rings on a horizontal plane, one for clockwise (the 'Blue Ring') and the other for counter-clockwise (the 'Yellow Ring') beams. The rings are oriented so that they intersect with one another at six locations (four of which are associated with experiments) along their 3.8 km circumference. 1740 superconducting magnets are required in order to bend, focus and steer the beams to a co-linear path for head-on collisions.
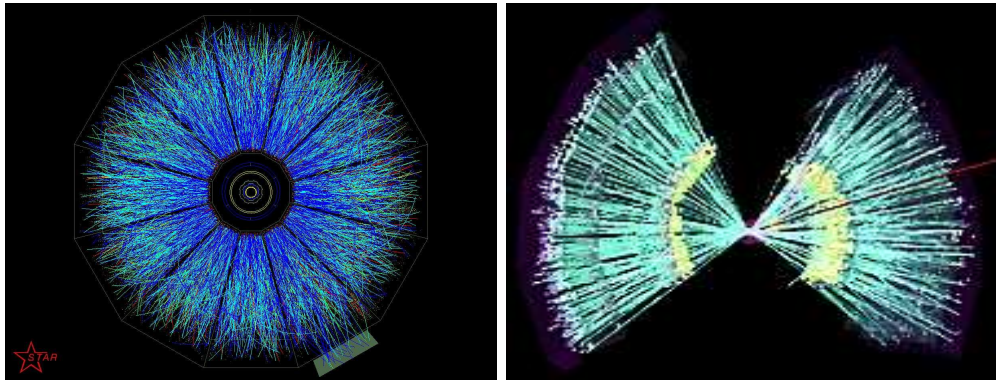
Figure 2.2: Au+Au collision as seen by the STAR (left) and PHENIX (right) detectors.

2.3   The RHIC Detectors

There are two major detector facilities (STAR and PHENIX) and two smaller experiments (PHOBOS and BRAHMS). In Figures 2.2 and 2.3, we present visual representations of data from all four detectors as recorded during gold-gold collisions.

The BRAHMS (Broad RAnge Hadron Magnetic Spectrometer) experiment was created to measure charged hadrons over the widest possible range of rapidity and transverse momentum. It consists of two magnetic spectrometers, one covering the forward and the other the central region of the collision phase-space. It also has a series of global charged hadron detectors (beam-beam counters, centrality detectors etc) for event characterization [43].

The PHENIX experiment (Pioneering High Energy Nuclear Interaction eXperiment) is one of the two large experiments currently taking data at RHIC [44]. With its three magnetic spectrometers and two Muon Arms subsystems (consisting of Muon Identifier and Muon Tracker), PHENIX measures electron and muon pairs, photons, and hadrons with excellent energy resolution.

The PHOBOS detector is capable of measuring charged particle densities over the full 4π solid angle using a multiplicity detector, and measures identified charged particles near mid-rapidity in two spectrometer arms with opposite magnetic fields [45]. The minimization of material between the collision vertex and the first layers of silicon detectors aims at the detection of charged particles with very low transverse momenta. This and the ability to record all interactions (unbiased running) are the
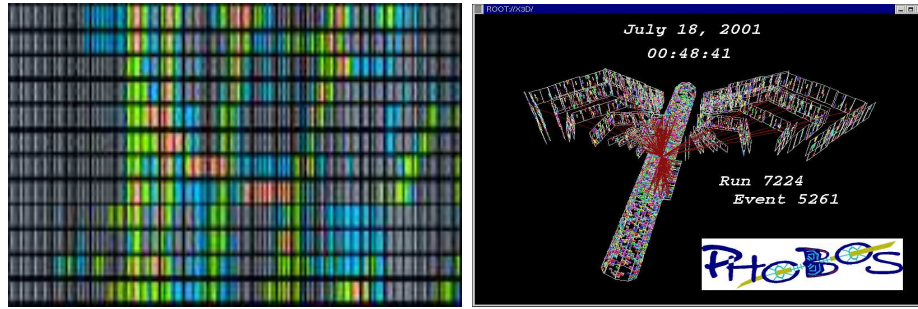
Figure 2.3: Au+Au collision as seen by the BRAHMS (left) and PHOBOS (right) experiments.

two unique feature of the PHOBOS experiment.

2.4 The STAR Detector

The Solenoidal Tracker at RHIC (STAR) was designed primarily for measurements of hadron production over a large solid angle, featuring detector systems for high precision tracking, momentum analysis, and particle identification in a region surrounding the center-of-mass rapidity [46]. The large acceptance of STAR (complete azimuthal symmetry $\Delta\phi = 2\pi$ and a pseudo-rapidity range $|\eta| < 4$.) makes it particularly well suited for single event characterization of heavy ion collisions and for the detection of hadron jets. Figure 2.4 shows a cutaway side view of the STAR detector as it was configured for the 2003 RHIC run, when the data used in this analysis were collected. Its main components are a large Time Projection Chamber (TPC), a Silicon Vertex Tracker (SVT), two smaller radial Forward and Backward TPCs (FTPCs), a Time of Flight patch (TOF) and an Electromagnetic Calorimeter (EMC) inside a $0.5\,\mathrm{T}$ magnetic field.
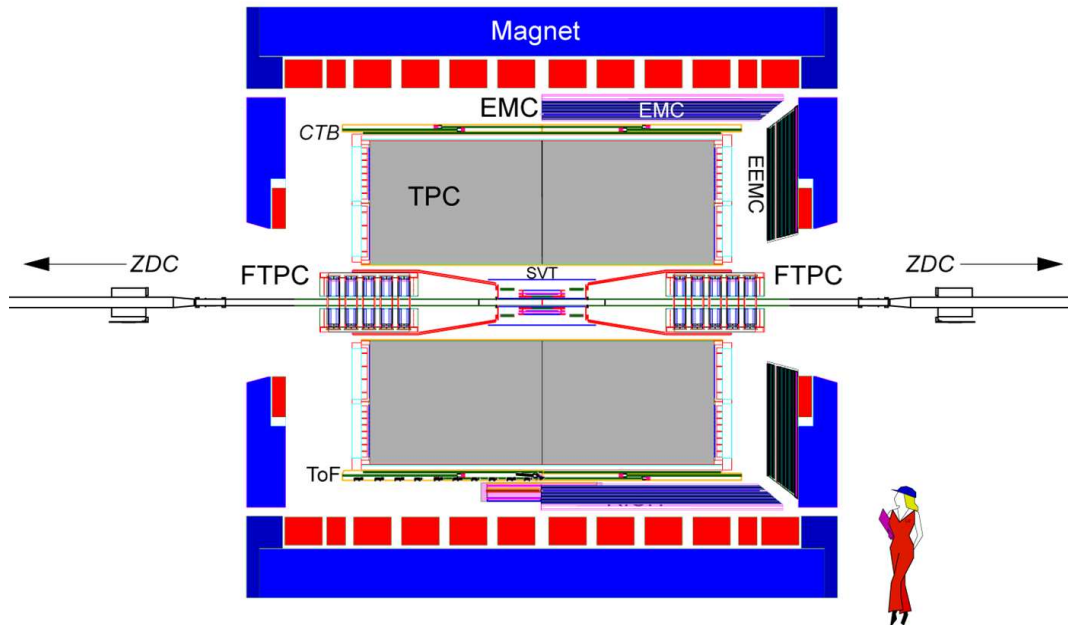
Figure 2.4: Cutaway side view of 2003 STAR Detector setup.

2.4.1   Trigger Detectors

The relatively slow readout time of the TPC, as compared to the event rates, makes it necessary to use an event selection mechanism, a trigger system. The STAR trigger system is a multi-level trigger system and is based on digitized input from fast and slow trigger detectors, signals which are analyzed at the RHIC crossing rate (10 MHz) [47]. This information is used to determine whether or not to accept an event and to initiate the Data AcQuisition (DAQ) readout cycle for the slower detectors (which provide information about the momentum and particle identification). With RHIC's peak designed luminosity for Au+Au collisions ($10^{27}\,\mathrm{cm^{-2}s^{-1}}$), the rate for minimum-bias[1] triggers is about $10{,}000\,\mathrm{s^{-1}}$. Since the event readout chain could

---

[1]A minimum-bias trigger is one that accepts any nucleus-nucleus collisions. In practice, very peripheral collisions are the most difficult to trigger on, since very few particles might be emitted, and there is an uavoidable bias against such events. A good min-bias trigger tries to keep this bias as small as possible.

record events only at rates up to about 100 Hz, the fast detectors have to provide means to reduce the rate by 2–3 orders of magnitude. Interactions are therefore selected, based on the distributions of particles and energy information from the trigger detectors (Figure 2.5): Central Trigger Barrel (CTB), Beam Beam Counter (BBC), Zero Degree Calorimeter (ZDC), Barrel Electromagnetic Calorimeter (BEMC), Endcap Electromagnetic Calorimeter (EEMC) and Forward Pion Detector (FPD). For example, in Au+Au collisions, different centrality classes of events are selected according to their particle multiplicity in the central region since more central events will have more nucleons participating in the collisions and therefore more particles produced. In the same picture one might trigger on the total number of spectator neutrons as measured in the two beam calorimeters (ZDCs).

The trigger system is divided into different layers with level 0 being the fastest while levels 1 and 2 are slower, since they use more detailed information. STAR has also a third level trigger (L3), which bases its decision on the complete, online reconstruction of the event. This particular trigger includes also a display which permits the visual inspection of the events almost in real time (Fig. 2.6).

Zero Degree Calorimeter

The ZDCs (West and East) are hadronic calorimeters located at $18\,\mathrm{m}$ from the IP (interaction point), centered at 0° and covering a solid angle of $\Delta\Omega < 2\,\mathrm{mrad}$. They are used to determine the energy of the remnant (spectator) neutrons in the forward direction from the breakup of the nuclear fragment.
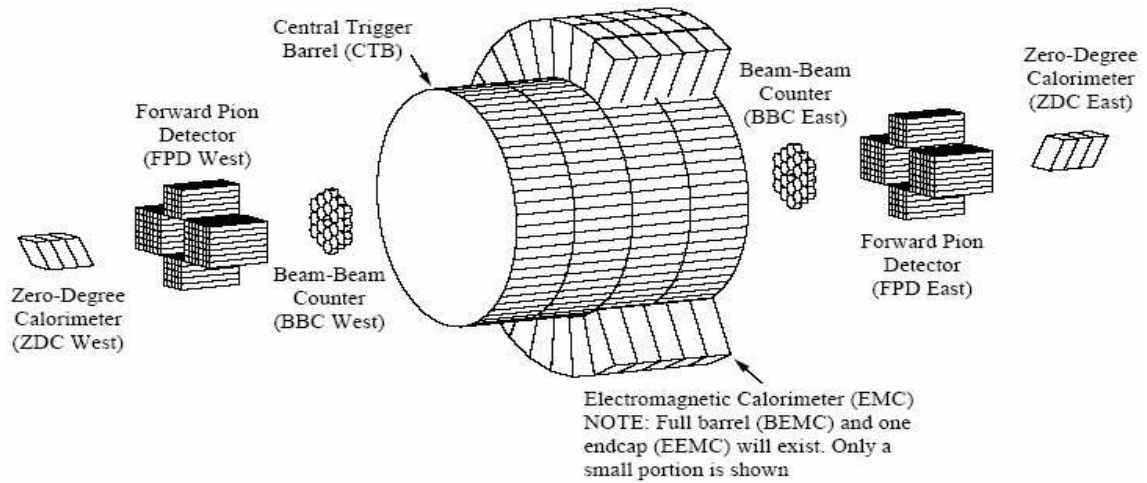
Figure 2.5: STAR trigger detectors.
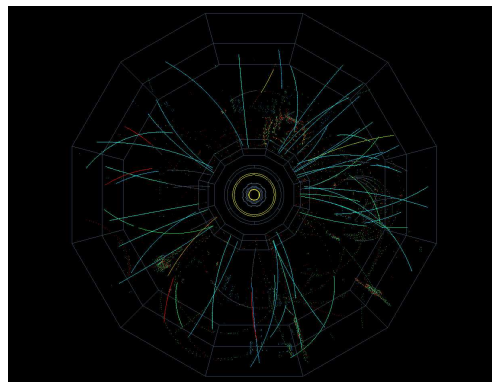
Figure 2.6: Level 3 trigger display: d+Au collision in 2003 run.

The Central Trigger Barrel and Beam Beam Counters

The CTB consists of 240 scintillator slats arranged around the TPC (Time Projection Chamber) and its signal is proportional to charged particle multiplicity in the pseudo-rapidity range $-1 < \eta < 1$ and over all azimuthal angle ϕ. There are 2 Beam-Beam Counters [48] wrapped around the beam-pipe, one on either side of the TPC. The timing difference between the two counters locates the primary vertex position. This trigger detector was mainly introduced to deal with the p+p collisions where the mid-rapidity multiplicity is much lower than in heavy ion collisions. For

example, in non-single-diffractive (NSD) inelastic collisions, after both protons break up, the produced particles are focused in the forward region. So, in order to trigger on these events, one needed a sensitive detector in the region close to the beam in the forward direction. The BBCs are placed at $\pm 3.5\,\mathrm{m}$ from the IP, and cover a region in pseudo rapidity of $2.1 < \eta < 3.4$.

Electromagnetic Calorimeters

The Endcap (EMC) and the barrel (BEMC) calorimeters make a good system which allows the measurement of transverse energy of events, and trigger on and measure high transverse momentum photons, electrons and electromagnetically decaying hadrons.

Barrel Electromagnetic Calorimeter

The BEMC is a lead-scintillator-based sampling electromagnetic calorimeter surrounding the CTB and TPC [53]. It measures neutral energy in the form of produced photons by detecting the particle cascade when those photons interact with the calorimeter. It covers the same region of space as the CTB: $|\Delta\eta| < 1$, $|\Delta\phi| < 2\pi$ and it is segmented into 4800 towers which for triggering purposes are grouped in sets of 16 to give 300 trigger patches each covering $(\Delta\eta,\ \Delta\phi) = (0.2,\ 0.2)$. It provides prompt charged particle signals which are essential in discriminating against pileup tracks in the TPC, arising from other beam crossing falling within the 40μs drift time of the TPC. This pileup effect is a serious concern/problem in the high luminosity p+p environment.

Endcap Electromagnetic Calorimeter

The Endcap EMC is also a lead-scintillator sampling electromagnetic calorimeter. It

covers the region between 1 and 2 in pseudorapidity and 2π in ϕ. There are 720 individual towers which are grouped together to form 90 trigger patches each covering $(\Delta\eta, \Delta\phi)=(0.2,0.2)$.

Forward Pion Detector

The FPD consists of 8 lead-glass calorimeters, four on each side of the IP of STAR: the Up, Down, North and South calorimeters. All calorimeters consist of arrays of lead-glass Cherenkov detectors, Up and Down 5×5 arrays, South and South 7×7 arrays. This detector detects very forward π^0s, it is used also as a local polarimeter for the polarized proton running.

2.4.2 Tracking Detectors

A Time Projection Chamber (TPC), a Silicon Vertex Tracker (SVT) and two Forward Time Projection Chambers (FTPC) all inside a solenoidal magnet, were the tracking devices in the 2003 run.

Forward Time Projection Chamber

The two cylindrical forward TPC detectors were constructed to extend the phase space coverage of the STAR experiment to the region $2.5 < |\eta| < 4.0$ ([51]). They measure momenta and product ion rates of positively and negatively charged particles as well as strange neutral particles.

Silicon Vertex Tracker

The SVT improves the accuracy of finding the primary vertex, and also the two-track resolution, and the energy-loss measurement resolution for particle identification. The SVT also enables the reconstruction of very short-lived particles (mainly strange and multi-strange baryons and D mesons) which have their decay vertex close to the primary vertex ([52]). It also expands the kinematical acceptance for primary particles to very low momentum by using independent tracking in the SVT alone for charged particles that do not reach the active volume of the TPC. The silicon detectors cover a pseudo-rapidity range $|\Delta\eta| \leq 1.0$ with complete azimuthal coverage.

Time of Flight Patch Detector

The TOFp was introduced to extend particle identification to larger momenta over a small solid angle. It covered a range in η from -1 to 0 and $\Delta\phi = 0.04\ \pi$. This detector made possible the identification of p and $\bar{p}$ up to 3 GeV/c transverse momentum for the dAu run. It is currently being replaced by a much larger TOF detector covering $|\Delta\eta| \leq 1.$ with full azimuthal coverage.

The Time Projection Chamber

The TPC is the primary tracking device of the STAR detector [50]. It records the tracks of particles, thus helping determine their momenta from their curvature in the magnetic field. It also identifies the particles by measuring their ionization energy loss (dE/dx). The Time Projection Chamber is located at a radial distance from 50 to 200 cm from the beam axis, providing complete coverage around the beam line ($\Delta\phi = 2\pi$), and tracking for charged particles within ± 1.8 units in pseudo-rapidity. With a length of 4.2 m and a diameter of 4m, it is the largest operating TPC in the
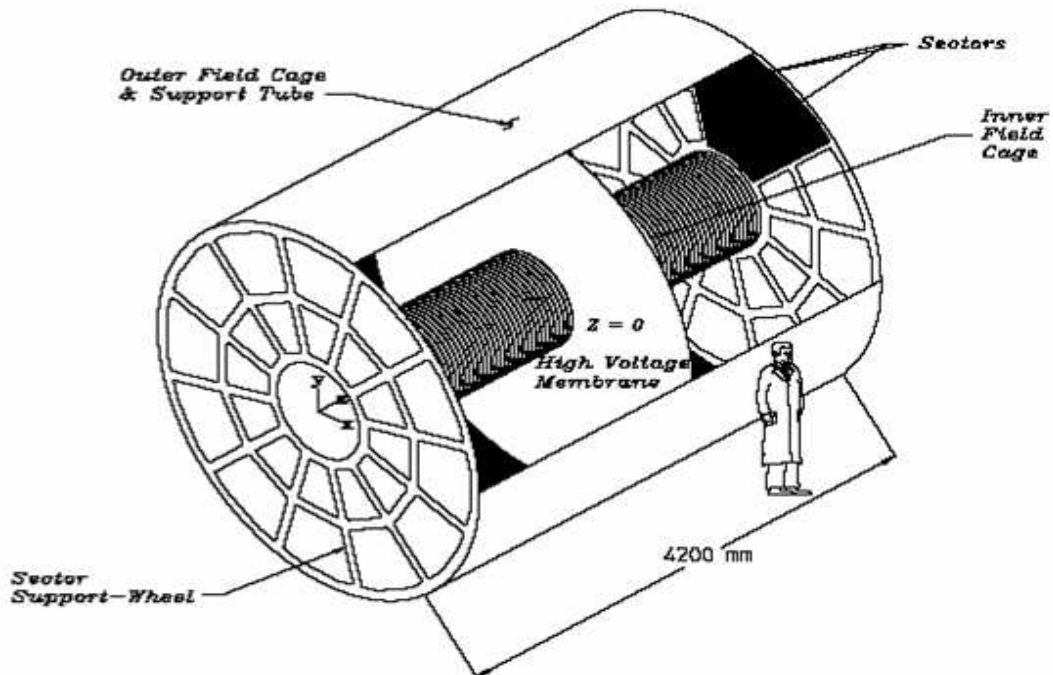
Figure 2.7: Schematic view of the STAR Time Projection Chamber (TPC).

world.

A schematic image of the TPC is shown in Figure 2.7. It sits in a solenoidal magnet that provides a uniform magnetic field of maximum strength 0.5 T (important for charged particle momentum analysis). The TPC volume is filled with P10 gas (10% methane and 90% argon), in a uniform electric field of $\approx 135\,\mathrm{V/cm}$. The trajectories of primary ionizing particles passing through the gas volume are reconstructed with high precision from the released secondary electrons which drift in the electric field to the readout end caps of the chamber. A large diaphragm (the Central Membrane) which splits the volume in half, is maintained at a high voltage with respect to the detection planes so that the liberated electrons drift away from the membrane to the closest endcap of the TPC, where their position in the r vs. ϕ plane is determined as a function of arrival time. The mean drift time constitutes a measurement of the
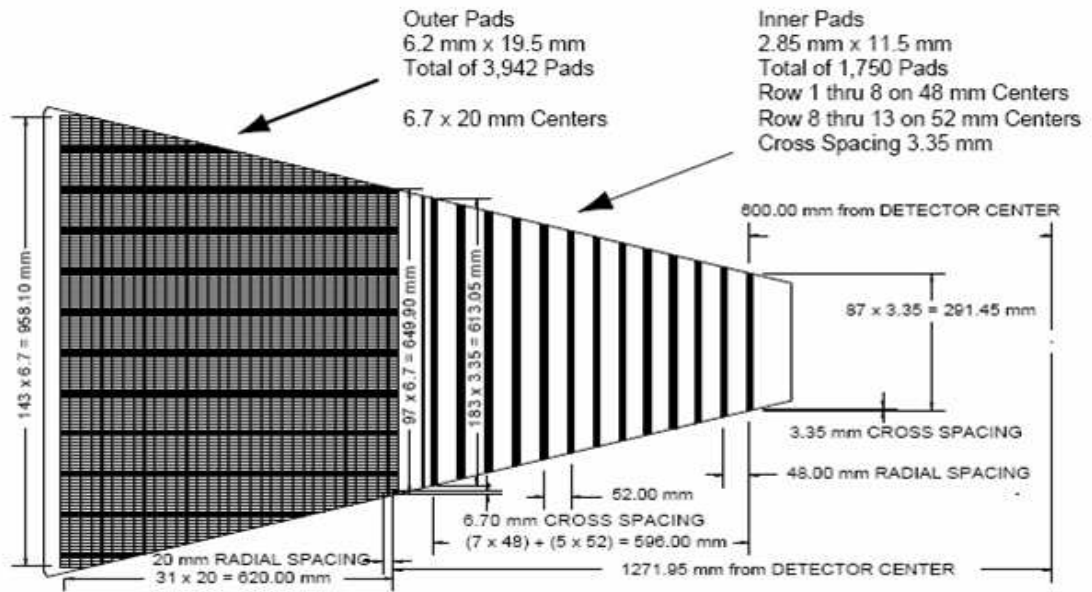
Figure 2.8: Schematic view of one of the 12 TPC sectors.

electron's point of origin along the z axis, yielding the third dimension. Each endcap of the TPC is radially divided into twelve sectors (having an angle of 30^0), which are further partitioned in an *inner* and an *outer* subsector. The inner subsector consists of 13 pad-rows and the outer of 32 pad-rows. The pads size (for details, see Figure 2.8) were chosen so that they provide good two-track spatial resolution. Additionally, the pads are closely packed to maximize the amount of charge collected by each of them, thus optimizing the dE/dx resolution. The spacing between pad rows is larger in the inner sector to cope with the higher hit density.

Chapter 3

Data Analysis

From the moment when raw data is registered by the tracking detectors to the moment a physical quantity like rapidity or transverse momentum is obtained, several steps have to be completed. We will review these steps in this chapter, starting with global event reconstruction and ending with the kink analysis technique particularities. We will focus on the reconstruction process inside the TPC, the main tracking detector data relevant to the analysis presented in this dissertation.

3.1 STAR Event Reconstruction

3.1.1 Hit and Track Reconstruction

The trajectory of a charged particle passing through the TPC is reconstructed by first finding ionization clusters called *hits*. A hit corresponds to the location where a charged particle has crossed a TPC pad row. The clusters are found in the two dimensional local coordinate system of the pad row, where the x direction is along the pad row and the y direction is the radial direction, perpendicular to the pad row. The z direction is along the beam line. Assuming that the hit is produced by a single track, its position is estimated by the centroid of the cluster. If two tracks come close together, then their clusters will overlap, in which case a cluster de-convolution algorithm[1] has to be applied in order to resolve separate hits where possible. Several corrections are applied and then the hits are recorded with the appropriate position in

---

[1] The algorithm tries to find the local maxima in the cluster and then de-convolute the cluster into individual hits.

the STAR global coordinate system. Information on the ionization energy associated with the hit is also recorded.

After the hits are found and their coordinates determined, a pattern recognition has to be performed to identify hits coming from the same charged particle (track). The track reconstruction algorithm starts from the outermost point of the TPC where the hit density is the lowest, and evolves inwards. It identifies points that are close in space, constructs segments from them (seeds), and then uses a helical extrapolation to add additional points to the segment, going both inward and outward from the initial segments. All possible hits that are close to the extrapolation are added. After this is complete, the newly found correlated points are fitted with a track model to extract information such as the momentum of the particle. The track model is, to first order, a helix. Second-order effects include the energy lost in matter, and multiple Coulomb scattering, which cause a particle trajectory to deviate slightly from a perfect helix.

3.1.2   Event Vertex Finding

The primary vertex (the ion collision point) is found by considering all the tracks reconstructed in the TPC and then extrapolating them back to the point of their distance of closest approach (DCA) from the beam-line. The position of the event vertex is then determined using χ^2 techniques on the track DCAs.

After track reconstruction and vertex finding, all tracks with DCA<3 cm are re-fitted, using the primary vertex as a fitting constraint. We end-up with two categories of tracks: 'global tracks' (all reconstructed tracks, including those coming from weak decays, other secondary processes etc.) and 'primary tracks' (tracks that include the

event vertex in their fit and therefore are considered to emanate from it).

3.1.3 Particle identification

The last important part of the event reconstruction chain is particle identification. There are two methods (relevant to this analysis) for this task: a) via ionization energy loss information in the TPC and b) by using topological reconstruction.

The dE/dx analysis is efficient especially for the low momentum particles but as the momentum rises, the bands for different particle masses merge together so it is hard to separate particles with high momenta. As an example, the pion and kaon bands can't be distinguished from each other above $700 \, \mathrm{MeV/c}$. A more powerful tool we use for reconstructing neutral and charged particle weak decays, thus allowing the parent particle type to be identified, is the topological reconstruction method.

For the neutral particles such as K_S^0 or Λ, the tracks that are not successfully refit to the primary vertex (hence *global* but not *primary* tracks) are used to identify the secondary vertex (so-called V_0) of their charged decay modes (Figure 3.1): $K_S^0 \to \pi^+\pi^-$, $\Lambda \to p\pi^-$ and $\overline{\Lambda} \to \bar{p}\pi^+$. These V_0s are also used to find multi-strange baryons ($\Xi^-, \overline{\Xi^+}, \Omega^-$ and $\overline{\Omega^+}$) which decay via a Λ or $\overline{\Lambda}$ and another charged particle. The charged kaons are also topologically reconstructed and we will present the details in the next section.
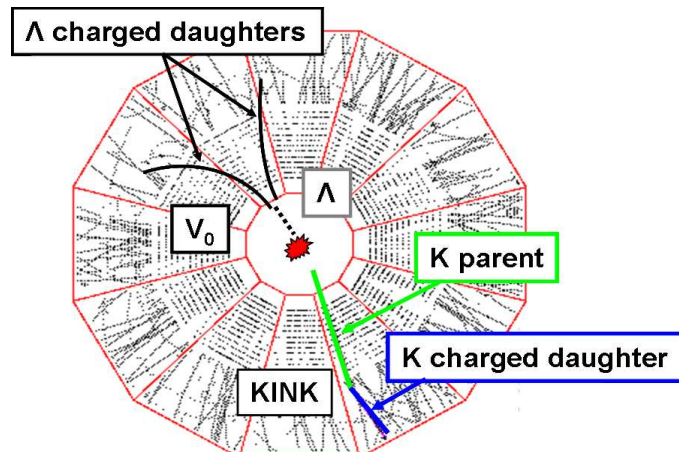
Figure 3.1: The 'kink' and the V_0 pattern which is searched for during the reconstruction process in the TPC

3.2 Kink Analysis

3.2.1 Kink Reconstruction

The kink reconstruction method is based on the fact that several of the charged kaon decay channels have the same pattern (Figure 3.1): the charged kaon (the parent), decays in one (or two) neutral particles(s) which are not detected (the daughter(s)) and one other charged daughter (observed track):

$K \rightarrow \mu\nu_\mu$ (63.5%), $K \rightarrow \pi^0\pi$ (21.2%), $K \rightarrow \pi^0\mu\nu_\mu$ (3.2%), $K \rightarrow \pi\pi^0\pi^0$ (1.7%).

A total distribution of all these channels is represented in black in Figure 3.2, where just one mass assumption ($K \rightarrow \mu\nu_\mu$) was used. The two colored distributions represent the decaying channels where the charged daughter is a muon (red) and pion (blue). Each of them presents the same features: two 'humps', a small one corresponding to the small-branching-ratio decays ($K \rightarrow \pi^0\mu\nu_\mu$ for the red curve and $K \rightarrow \pi\pi^0\pi^0$ for the blue curve) and one corresponding to the big-branching-ratio decays ($K \rightarrow \mu\nu_\mu$ red and $K \rightarrow \pi^0\pi$ blue).

The 'kink finder' starts by looping over all global tracks reconstructed in one event

and looks for pairs of tracks which have a certain pattern: where one track ends (the parent kaon candidate), the other track in the pair starts (the daughter candidate). All pairs for which the charge sign is different for the two tracks are discarded. In order to minimize the combinatorial background created by randomly crossing tracks (which is bigger the close we get to the primary vertex), the first sorting criterion imposed by the kink maker (the software package responsible for finding the kink candidates) is that the kaon decay vertex has to be in a certain fiducial volume. This volume is chosen to lie entirely in the outer TPC region, and it covers, the region between 133 cm and 179 cm from the primary vertex. Several other cuts (besides the one which requires that the kink vertex is in the fiducial volume) are applied on the track pairs in order to select the kink candidates (see also Ref. [55] for details): three distance-of-closest-approach (DCA) cuts (distances between parent and daughter, daughter and primary vertex, parent and primary vertex), decay angle of the parent, orientation of the parent and daughter tracks with respect to the primary vertex (the parent track has to point back to the primary vertex but not the daughter). For each kink candidate found, a mass hypothesis is given to both parent and daughter tracks on the basis of an invariant mass analysis. Since charged pions have $\sim100\%$ branching ratio for the decay channel $\pi \to \mu\nu$, the same channel as charged kaons and hence same track decay topology in the TPC, we expect that using this track based particle-finding algorithm to reconstruct both kaons and pions, so that in the end, we have as 'kink' parent candidates K^+, K^-, π^+ and π^-. The invariant mass analysis tests only the channels where in the final state there are only 2 particles (the kaon channels $\pi\pi\pi^\pm$ and $\pi\mu\nu$ are not tested explicitly), so we expect that some of these kaons to be misidentified as pions. A careful analysis is necessary in order to
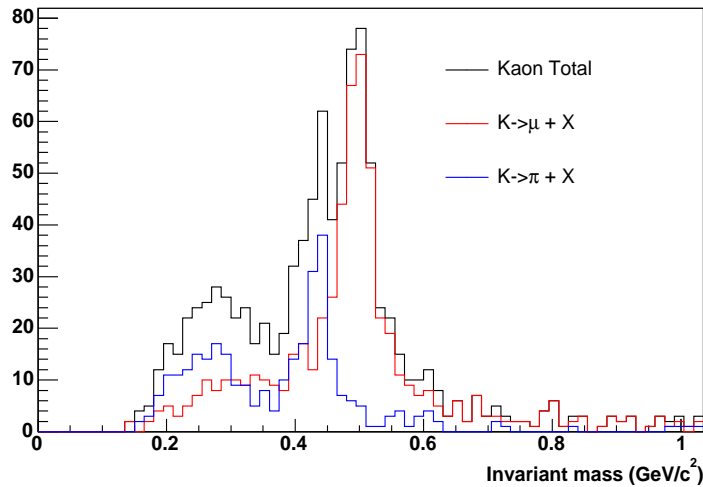
Figure 3.2: Kaon invariant mass, assuming the μ mass hypothesis.

trim the kink kaons from the kink pions.

Once the kink candidates are selected, they are stored for further analysis with infor-
mation about the kink vertex, parent and daughter tracks. These are the 'kinks' that
are the starting point for the analysis of a certain collision. However, several other
cuts have to be applied in order to obtain a cleaner charged kaon signal, meaning a
good signal over background ratio. These additional cuts, which will be presented in
detail later, are performed at the final analysis level and not during the event recon-
struction phase.

3.2.2   Cut Tuning

In order to obtain a good signal over background ratio for charged kaons, one has
to apply tight cuts on the kinks stored after the event reconstruction stage. We use
events from HIJING [57] (a Monte-Carlo-based event simulator) to estimate the effect
of each cut on the signal and on different sources of background. Taking this approach,
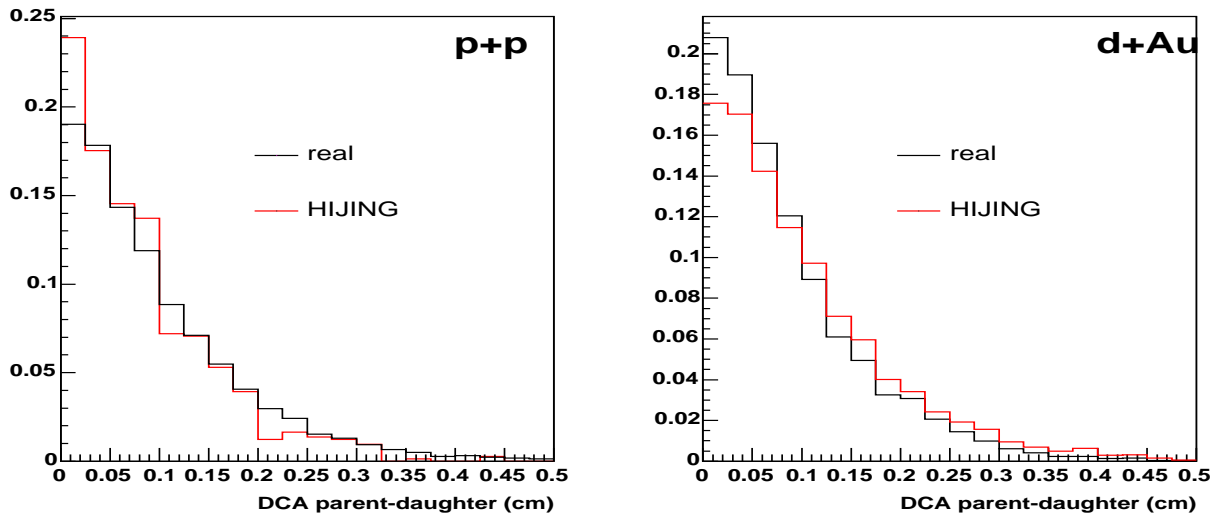
Figure 3.3: Kaon decay angle. Final kaon signal comparison, between real (black) and simulated data (red), after all analysis cuts are applied.

we have control on what is signal and what is background. The terminology used is the following: we call *signal* those kinks that are associated with Monte Carlo (MC) kaon decays; *correlated background* refers to kinks which are associated with other than kaon decay MC processes, and finally, *combinatorial background* refers to those kinks not associated with any MC physical process. We begin by showing a comparison between the output of the simulation tool used to tune the cuts (HIJING) and real data. The kaon decay angle and the distance of closest approach (DCA) between the parent kaon and its daughter are plotted in Figures 3.3 and 3.4 respectively. All analysis cuts are applied in these plots, on both real and simulated data. Since in real life, we can't have a 100% pure sample but there will always exist some background, the HIJING output plotted has the final signal and the remaining background (which escaped our cuts) added together. The qualitative agreement between the two results gives us confidence in the simulation.
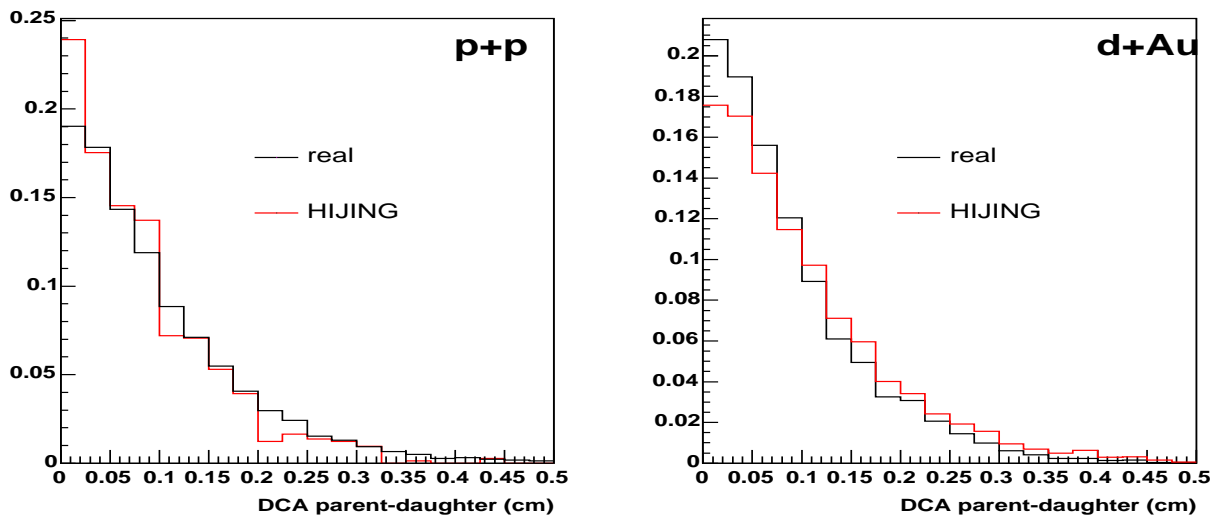
Figure 3.4: DCA parent-daughter. Final kaon signal comparison, between real (black) and simulated data (red), after all analysis cuts are applied.

There are two main background sources for kaons. The most important one (which makes the correlated background) is mostly the charged pions, for reasons explained in the previous section. The second source, which builds 'the combinatorial background', is randomly intersecting tracks in the TPC which are reconstructed as kinks. To have an idea about the background level, we present in Figure 3.5 an invariant mass plot of the 'raw' kinks (with only the cuts applied at the kink-finding stage), which is calculated assuming just the principal decay channel for the kinks, $K \rightarrow \mu\nu_\mu$. Invoking the conservation of 4-vector momentum (p_X^μ)for the 2-particle decay,

$$(3.1) \qquad\qquad p_K^\mu = p_\mu^\mu + p_{\nu_\mu}^\mu$$

which can be translated in

$$(3.2) \qquad\qquad (E_K, \overrightarrow{p_K}) = (E_\mu + E_\nu, \overrightarrow{p_K}).$$
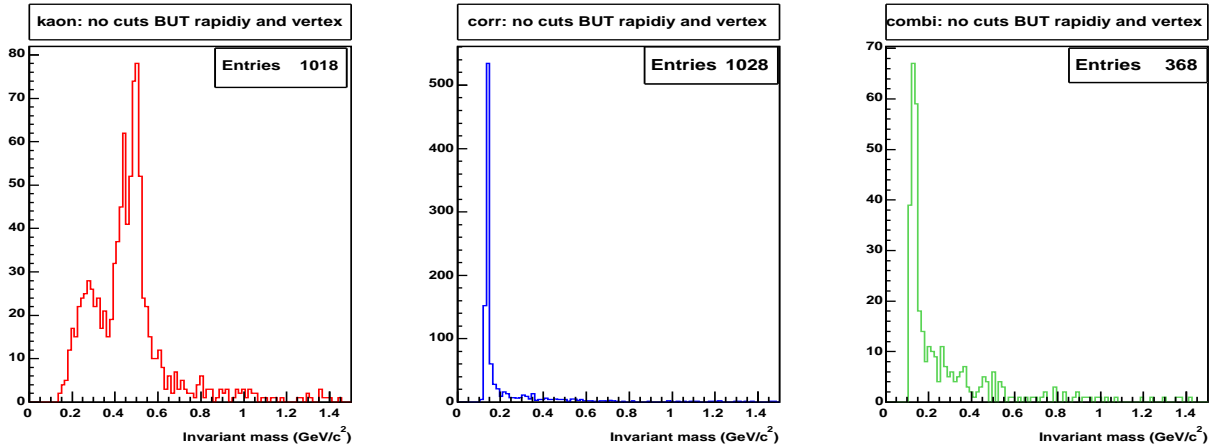
Figure 3.5: Monte Carlo analysis of the cuts for p+p; invariant mass distribution for signal and background *before* any cuts are applied.

The kaon invariant mass is then

$$(3.3) \qquad M_K^2 = E_K^2 - \overrightarrow{p_K}^2 = (E_\mu + E_\nu)^2 - \overrightarrow{p_K}^2$$

Since $E_{\nu_\mu} \sim p_{\nu_\mu}$, Eq.3.3 gives

$$(3.4) \qquad M_K^2 = (E_\mu + p_\nu)^2 - \overrightarrow{p_K}^2$$

where $\overrightarrow{p_{\nu_\mu}} = \overrightarrow{p_K} - \overrightarrow{p_\mu}$ and $E_\mu = \sqrt{p_\mu^2 + m_\mu^2}$.

We observe clearly the main 3 decay channels (only one at the correct kaon mass position, 494 MeV/c^2, and the other two shifted, according to our decay kinematics assumption) but also a huge peak positioned at the pion mass, 135 MeV/c^2. After applying the cuts, in Figure 3.6, the background level is drastically reduced.

Since in this dissertation we concentrate on the p_T spectra and on the results involving the p_T spectra, we plot also the background distribution function of transverse momentum before and after all the cuts are applied, for both p+p (Figure 3.8) and d+Au (Figure 3.7) data samples. In the raw distributions, we can see that the correlated background (mostly pion contamination) is concentrated at low p_T before the
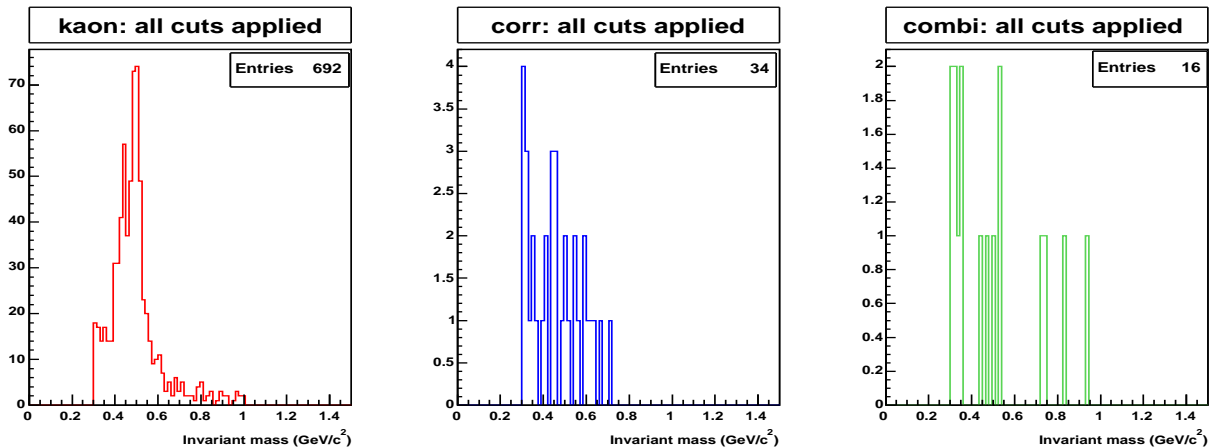
Figure 3.6: Monte Carlo analysis of the cuts for p+p; invariant mass distribution for signal and background *after* all the cuts are applied

cuts, the ratio of signal over all background being at all times smaller than 4. After applying the cuts, the background is much smaller and more uniform, the influence on the final results being minimal: in the low p_T region, essential for calculating the spectra characteristics ($p_T, \langle dN/dy \rangle$), is negligible, while is larger as a percentage, but still adequately small at higher p_T.

We present in the following the analysis cuts, their physics motivation and their impact on the signal to background ratio.

Kaon Decay angle (θ) cut: This is of the two most important cuts for trimming the pions (the other one is the dE/dx cut) and it is based on the fact that if a decaying particle has a high enough momentum, the Lorentz boost that it provides to its daughters limits the possible decay angle in the laboratory frame. We can see this by analyzing Equation 3.5

$$(3.5) \qquad \tan(\theta^{lab}) = \frac{p_T^{lab}}{p_z^{lab}} = \frac{p_T^{CM}}{\gamma(p_z^{CM} + \beta E^{CM})}$$

where θ^{lab}, the decay angle of the daughter in the laboratory frame is expressed in
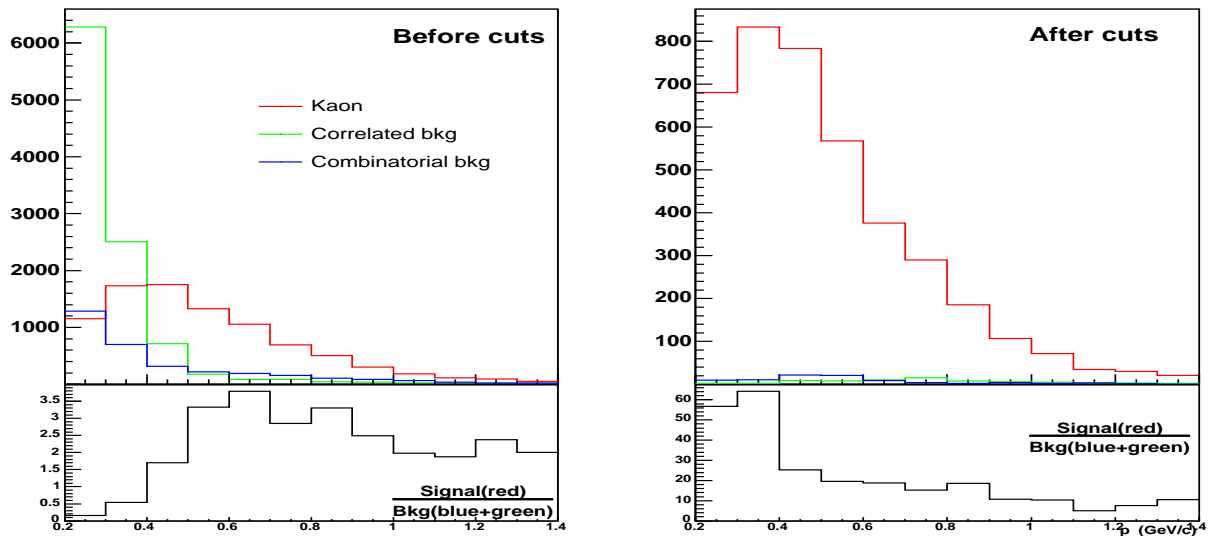
Figure 3.7: d+Au simulation analysis of the signal and background, before (left) and after (right) the analysis cuts are done.

terms of daughter momentum (transverse momentum p_T, longitudinal momentum p_z) and in terms of Lorentz factors $\beta = \frac{p}{E}$ and $\gamma = \frac{1}{\sqrt{1-\beta^2}}$ (for β and γ, the parent momentum and energy are used).

For a certain momentum of the parent (hence γ, β fixed), the angle depends only on the daughter momentum (p_T^{CM} and p_z^{CM}) and mass ($E^{CM} = \sqrt{m^2 + p_T^{CM}}$), all in the center of mass of the kaon decay. But since the identity of the daughters is the same for pions and for the main decay channel of the kaons ($K \rightarrow \mu\nu_\mu$), the decay kinematic difference is brought by the parent characteristics. We can look at the dependence of the decay angle on the Lorentz boost factor (Equation 3.6)

$$(3.6) \qquad \tan|\theta| \sim \frac{1}{\beta\gamma} = \frac{\sqrt{1-\beta^2}}{\beta} = \sqrt{\frac{E^2}{p^2} - 1} = \frac{m}{p}$$

Since $m_\pi < m_K$, then $\theta_{pi} < \theta_K$. This is to say that for a given parent momentum,
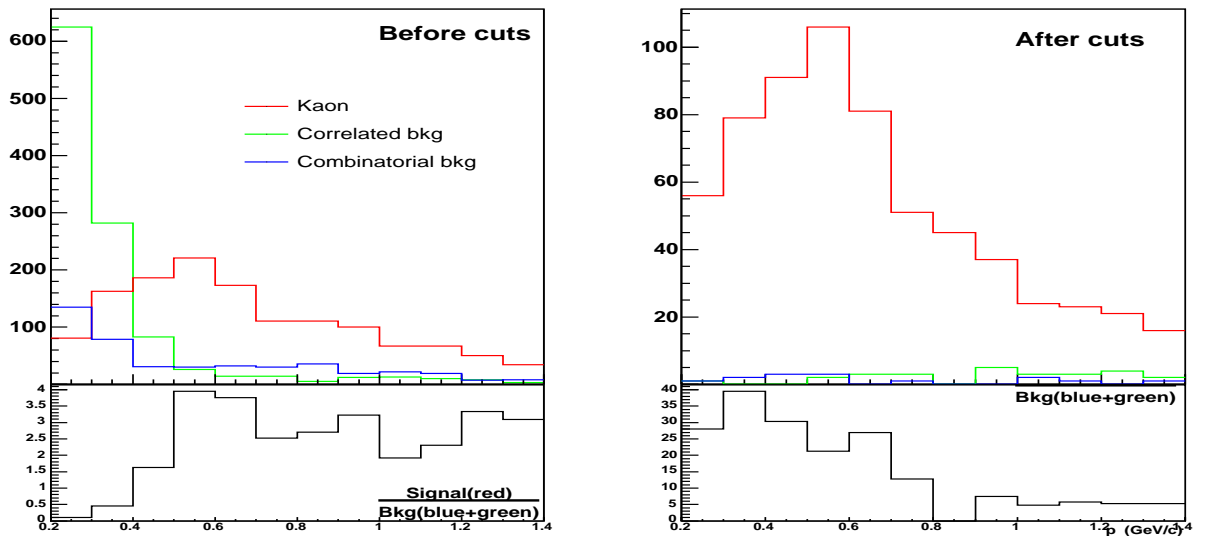
Figure 3.8: p+p simulation analysis of the signal and background, before(left) and after (right) the analysis cuts are done.

there is a maximum possible decay angle for pions decaying into a muon and the corresponding neutrino. We use this value (for each parent momentum) to cut the pions from our kink sample (Figure 3.9).

Energy Loss(dE/dx) cut: As the particles traverse the TPC, they ionize the TPC gas and lose energy. The energy loss (in units of eV/cm here) is parameterized by the Bethe-Bloch formula, given in Equation 3.7,

$$(3.7) \qquad -\frac{dE}{dx} = \frac{e^2(Ze)^2 n_e}{4\pi\epsilon_0^2 m_e(c\beta)^2}[\ln(\frac{2m_e(c\beta\gamma)^2}{I}) - \ln(1-\beta^2) - \beta^2]$$

where m_e is the electron mass and e its charge, Ze is the hadron charge, n_e is the electron density in the medium and I is the average ionization energy of the material. We cut around the ionization curves for kaons removing in this way very little of the signal kaons but an important part of the background (Figure 3.10). The cut is done
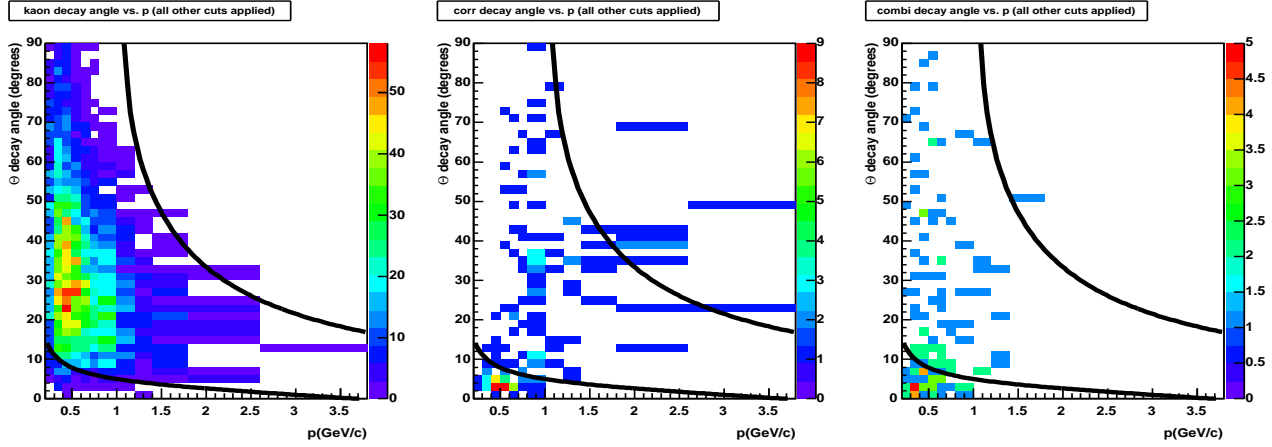
Figure 3.9: Decay angle vs. parent momentum; all cuts are applied except the decay angle
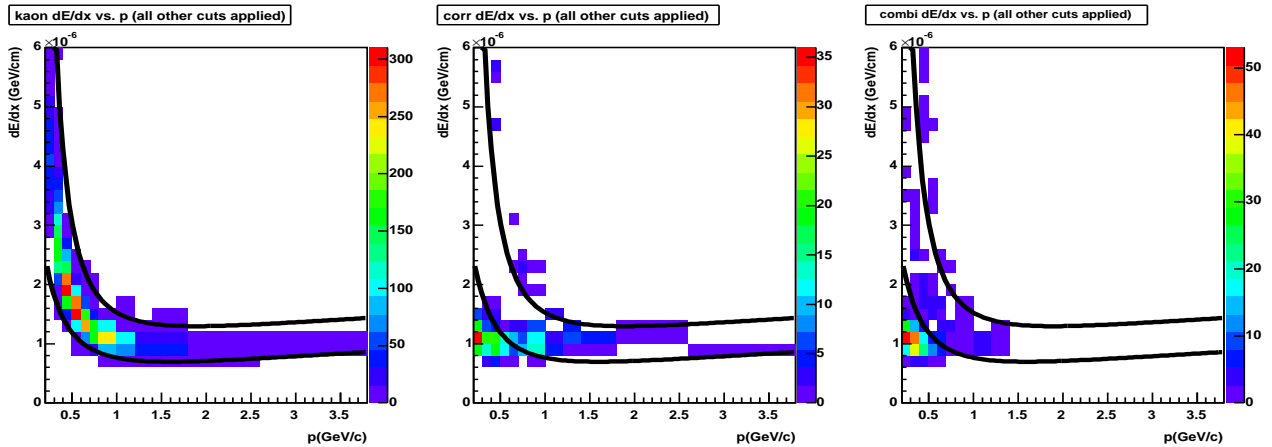
Figure 3.10: Energy loss vs. parent momentum; all cuts are applied except dE/dx
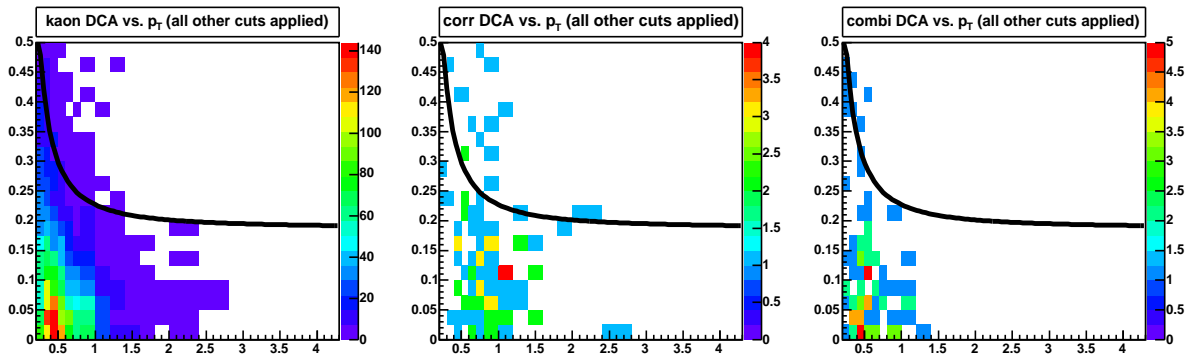
Figure 3.11: DCA parent-daughter vs. parent p_T; all cuts are applied except DCA cut.

for momentum smaller than $500\,\mathrm{MeV/c}$, the region where the pion and kaon bands are clearly separated.

Parent-Daughter DCA cut: The DCA cut is momentum dependent: the higher the p_T, the straighter is the track and smaller the DCA value. The method used to determine the cut is identical to the one described in [65]. Its functional form is $\mathrm{DCA_{cut}}(p_T) = A + B/p_T{}^C$ with A, B and C parameters. The DCA distribution versus transverse momentum of the parent is plotted in Figure 3.11 for dAu, with all cuts applied except the DCA cut which is represented by the curve.

Local (TPC) angle cut: We impose a condition on the kink vertex position to be not within 2.5 degrees from the sectors boundaries. In this way we eliminate the split tracks between two sectors which are reconstructed as kinks.

Daughter Momentum cut: We cut kinks for which the daughter momentum is lower than $100\,\mathrm{MeV/c}$. Using this cut, we remove part of the background produced by randomly intersecting tracks.

3.2.3 Corrections

There are three types of corrections that we applied in order to obtain the final spectra: one for the remaining background ("contamination" corrections), one to account for the limited geometrical coverage of the detector or other limitation of the reconstruction ("acceptance and efficiency" corrections), and finally a correction for the missing vertices ("vertex" corrections).

Contamination corrections

The starting point for the correction are the HIJING plots in Figures 3.8 and 3.7, in which are plotted the signal and background distributions after all the analysis cuts are applied, as a function of p_T. The formula used for determining the contamination correction factors, for a p_T bin i, is given by the following formula:

$$f^i = (\frac{\text{kaon}_{\text{left}}}{\text{kaon}_{\text{left}} + \text{bkg}_{\text{left}}})^i$$

where 'left' refers to the signal and background that remained after the all the analysis cuts are applied. Because the background shape is slightly different for positive and negative kaons (especially at low p_T), we calculated these factors separately for K^+ and K^-.

Acceptance and Efficiency corrections

These corrections are done using the heavy-ion collision simulator HIJING [57], a detector response simulator (GEANT [56]) and a technique called *embedding*. The technique is as follows: Monte Carlo (MC) particles are generated, propagated and decayed in the simulated STAR setup, and GEANT determines how the generated particles interact among themselves and with the detector material. The TPC Response Simulator (TRS) generates an output in the same format as the real data. These digital signals are mixed then with signals from real events and reconstructed.
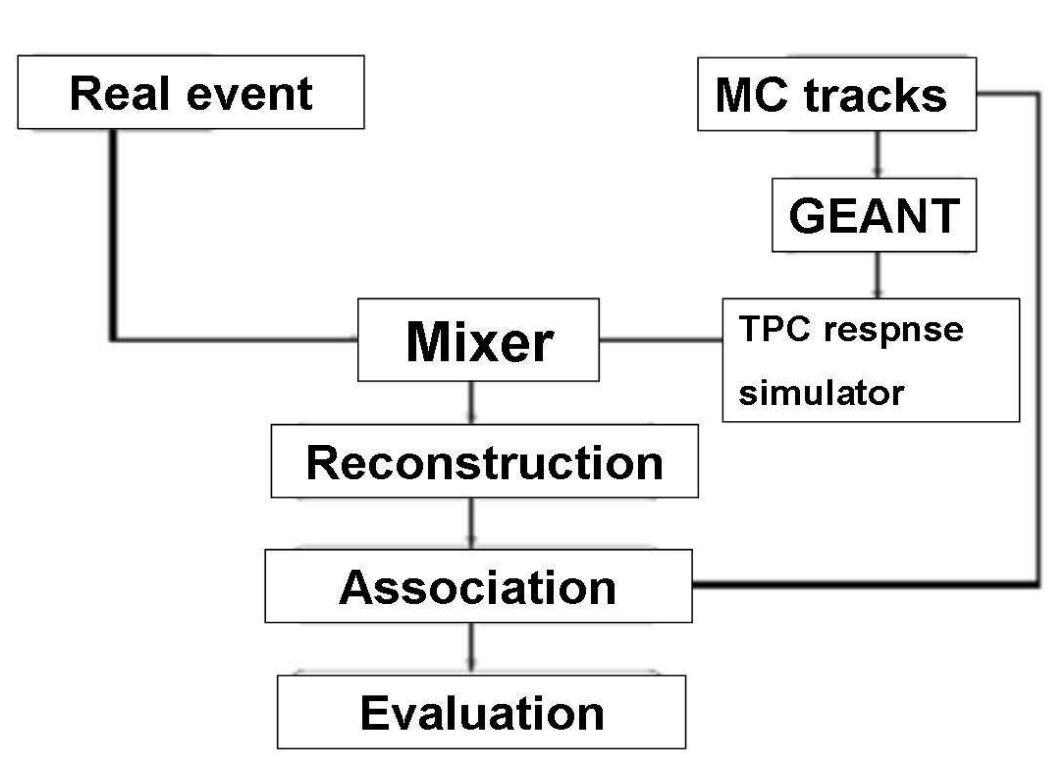
Figure 3.12: Logic diagram for the embedding process.

In the end, an association algorithm[2] tags each simulated track that is successfully reconstructed. The embedding process is schematically presented in a logic diagram in Figure 3.12. Using this method, we are able to monitor how a simulated track propagates through the detector and is reconstructed by the event reconstruction chain, in an environment which is very close to the real one.

So, what we are interested in is what percentage of all charged kaons produced in the collision are reconstructed by using the 'kink' method. We have to account for the kaons that do not leave a measurable signal in any sensitive region of the detector and those that decay before they reach the detector. This sort of correction is called *acceptance correction* and it is defined in terms of the embedding method as

---

[2]An initial simulated and embedded hit/track is associated with a reconstructed hit/track according to the best 'association' criterium: the closest MC hit/the highest number of common hits.

d+Au (0-20)%	d+Au (20-40)%	d+Au (40-100)%	d+Au (0-100)%
$\sim 100\%$	$\sim 100\%$	$\sim 88\%$	$\sim 93\%$

Table 3.1: Vertex efficiency in p+p and d+Au collisions.

the number of kaons that decayed in the fiducial volume over all the kaons that were embedded.

(3.8)

$$\text{Acceptance}_{\text{correction}} = \frac{\text{all MC Kaons that GEANT decayed in the fiducial volume}}{\text{all MC Kaons that were embedded}}$$

We also have to account for the charged kaons that decayed in the fiducial volume but weren't found by the kink finder or haven't passed the analysis cuts. We call this *efficiency correction* and define it as the ratio between all charged kaons that passed the kink cuts (the kink finder and analysis level cuts) over all the kaons that decayed in the fiducial volume

(3.9)

$$\text{Efficiency}_{\text{correction}} = \frac{\text{MC Kaons that passed the kink cuts}}{\text{all MC Kaons that GEANT decayed in the fiducial volume}}$$

Vertex corrections

An additional correction had to be applied to account for primary vertex reconstruction inefficiency, i.e. cases in which a vertex existed but was not reconstructed. The values used for correcting for missing vertices are listed in Table 3.1 . For dAu, the correction is applied to the total number of events (Nevt) used to get the per event yield, i.e., the corrected number of events is $\text{Nevt}_{corrected} = \text{Nevt}(1 + \text{eff})$.

In the case of the pp data sample, the primary-vertex-finding correction was more elaborate. For the missing vertices, a correction factor was calculated for each p_T bin function of the event multiplicity [58]. In addition, because in the

very 'rarefied ' track medium created in p+p collisions, fake vertices can be reconstructed, a correction for this effect has to be done and it was parameterized as corrFake(p_T) = $1 - 0.05811 exp(0.07505/p_T)$. This correction was applied to the final (corrected for acceptance, efficiency etc) spectra. Because the effect of missing vertices is opposed (increases the final yield) to the one of fake vertices (which decreases the yield), they do annihilate each other in some sense and because of that, there is only a small difference (less than 10%), within the statistical errors, between the case when we use a global correction factor (as in dAu case).

One more note related to the p+p collisions for which the Non-Single Diffractive (NSD) cross section was calculated to be ∼30±3.5 mb. This was obtained by doing a Vernier Scan and using the PYTHIA simulation of the BBC acceptance [59]. This is what was measured and differs from the total cross section which is 42 mb. The number of events normally used to normalize the p+p spectra is thus from NSD. Since most (> 95%) of the single diffractive events don't produce particles at mid-rapidity, this means that there are a lot of "empty pp collisions" which we need to count in the number of events. There are actually a factor of 42/30=1.4 total interactions which we have to take in consideration. Though all the pp spectra presented here are still based on NSD, the correction factor 1.4 was used for all plots where p+p data and Au+Au or d+Au data were combined together with N_{coll} or N_{part} values, since for calculating these numbers, in the Glauber model the *total* p+p cross section was used.

3.2.4 Systematic errors

Four sources of systematic errors were investigated : analysis cuts variation, background subtraction, fitting methods and vertex correction methods.

Hadron		dAu	pp
K^+	$< p_T >$	0.012	0.006
	$\langle dN/dy \rangle$	0.017	0.004
K^-	$< p_T >$	0.024	0.006
	$\langle dN/dy \rangle$	0.022	0.004

Table 3.2: The absolute systematic errors on the final $\langle dN/dy \rangle$ and $\langle p_T \rangle$ values due to the cuts applied.

The relation used for calculating the systematic error is given by Equation 3.10 [60], where x_i is the result of the ith (of the total of n) set of cuts used and x is the value for the default set of cuts.

$$(3.10) \qquad s^2 = \frac{1}{n-1} \sum_{i=1}^{n} (x_i - x)^2$$

The overall systematic error, was obtained by adding the three separate errors in quadrature:

$$(3.11) \qquad s_{total} = \sqrt{s_{cuts}^2 + s_{bkg}^2 + s_{fits}^2 + s_{vtx}^2}$$

Analysis cuts variation

The DCA, invariant mass, vertex position and phi local angle cuts were varied one at a time, spectra being fitted each time and $\langle p_T \rangle$, $\langle dN/dy \rangle$ values calculated. We summarize the final numbers in Table 3.2 .

Background subtraction

Since the simulation statistics were poor at higher p_T, the contamination factors had to be approximated above $1\,\mathrm{GeV/c}$: a constant factor, the same as at $1\,\mathrm{GeV/c}$, was used. Since both p_T and $\langle dN/dy \rangle$ values are driven by the spectra below $1\,\mathrm{GeV/c}$, we expect that a variation of the correction factors above this p_T limit to have a small

Hadron		dAu	pp
K^+	$< p_T >$	0.011	0.013
	$\langle dN/dy \rangle$	0.007	0.005
K^-	$< p_T >$	0.007	0.001
	$\langle dN/dy \rangle$	0.007	0.008

Table 3.3: The absolute systematic errors on the final dNdy and $\langle p_T \rangle$ values due to the background substraction methods.

influence on the final results. The way we convinced ourselves of this, was by not correcting at all for pp data set. Indeed the result confirms what we have concluded already in the previous sections, that the contamination is small, less than 3%. We list in Table 3.3 the numbers.

For the dAu data set, where the contamination can not be ignored, we used a different subtraction method, developed in [65] and successfully used on AuAu data. The basic idea is to use the real data itself to account for the background. The kinks with DCA$\leq$DCA$_{cut}$ were labeled as signal, and the rest as background. Then the spectrum of the rejected ('background') candidates is subtracted from the spectrum of the accepted candidates ('signal'), the result being the final spectrum that later will be corrected for acceptance and efficiency. Again, the difference between the two methods is less then 3%.

Fitting method source

Considering $dy = E/dp_z$, and integrating over ϕ, the relation between the theoretically calculated invariant cross section and the measured hadron spectra is given by Equation 3.12

(3.12)

$$E\frac{d^3\sigma}{dp^3} = E\frac{d^3\sigma}{dp_x dp_y dp_z} = \frac{d^3\sigma}{dp_x dp_y dy} \simeq \frac{d^3\sigma}{p_T dp_T dy d\phi} \simeq \frac{d^2\sigma}{2\pi p_T dp_T dy} \simeq \frac{d^2N}{2\pi p_T dp_T dy}$$
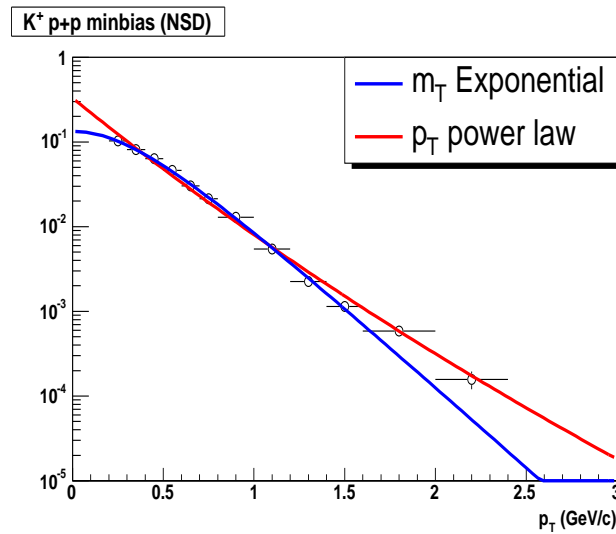
Figure 3.13: Simple power law and exponential fit of K^+ p+p minbias (NSD) spectrum

There are two widely-used fit functions (that reproduce the spectra) used for extracting the spectrum characteristics, $\langle p_T \rangle$ and $\langle dN/dy \rangle$: a function like a power law (pQCD inspired)

$$(3.13) \qquad f^{fit} = A[1 + \frac{p_T}{B}]^{-C}$$

and a 'thermal' one [62]:

$$(3.14) \qquad f^{fit} = De^{-\sqrt{(p_T^2 - m^2)/E}}$$

with A..E fit parameters. The power law function was at the first introduced empirically: it was noted that a power of 4/8 [61] is necessary to describe the spectra for mesons and baryons *above* 2 Gev/c.

The thermal distribution was introduced in order to describe the observed different spectral shapes for particles with different masses: the heavier the particle, the more 'curved' the spectrum at low p_T, an effect possibly caused by an explosive (as opposed to radiative) source and radial flow.
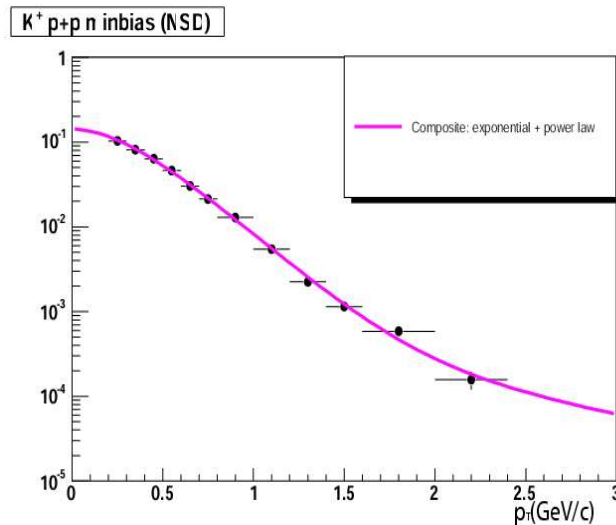
Figure 3.14: Fit of K^+ transverse momentum p+p minbias (NSD) spectrum, using an exponential fit at low p_T and a power law fit at high p_T.

Independent of the function used, the $\langle p_T \rangle$ and $\langle dN/dy \rangle$ values are given by $\langle p_T \rangle = \frac{\int 2\pi p_T f^{fit} p_T dp_T}{\int 2\pi f^{fit} p_T dp_T}$ and $\langle dN/dy \rangle = \int 2\pi f^{fit} p_T dp_T$. Neither of these two functions describes the data satisfactory for pp or dAu, see Figure 3.13. The power law fails at low p_T and the exponential at high p_T. Starting from this point, we used two alternative approaches, both giving similar results within a few percent. In the first approach, we constructed a "composite" function (Equation 3.15), with both components included. The fit agrees with the data over the whole p_T range, see Figure 3.14.

$$(3.15) \qquad A[1 + \frac{p_T}{B}]^{-C} + De^{-\sqrt{(p_T^2 - m^2)/F}}$$

In the second approach, we fit the spectra from the lowest p_T in the data ($0.2\,\mathrm{GeV/c}$) up to $1\,\mathrm{GeV/c}$ with the exponential function, fit the spectra above 1.5-3 $\mathrm{GeV/c}$ with the power law function, and then extract the fit function parameters. We will use these parameters to fix our fit functions in the regions where no data is available (below 0.2 and above $3\,\mathrm{GeV/c}$). In this way, the final numbers will be a combination of the results obtained in three momentum regions: 0.5-0.2 $\mathrm{GeV/c}$ (exponential function) +

Hadron		dAu	pp
K^+	$< p_T >$	0.008	0.006
	$\langle dN/dy \rangle$	0.004	0.001
K^-	$< p_T >$	0.024	0.011
	$\langle dN/dy \rangle$	0.006	0.002

Table 3.4: The absolute systematic errors on the final $\langle dN/dy \rangle$ and $\langle p_T \rangle$ values due to the fitting methods.

Hadron		dAu	pp
K^+	$< p_T >$	0.018	0.015
	$\langle dN/dy \rangle$	0.020	0.006
K^-	$< p_T >$	0.038	0.012
	$\langle dN/dy \rangle$	0.024	0.009

Table 3.5: Total absolute systematics errors for p+p and d+Au $\langle dN/dy \rangle$ and $\langle p_T \rangle$. The cuts, background fitting method and vertex correction systematic errors are combined, according to Eq. 3.12.

data points + above 3.0 GeV/c (power law). This method is particularly efficient (time saving), when the spectra are not quite smooth due to poor statistics and a fit to the entire spectrum would be difficult.

The final systematic errors associated with the fitting methods are presented in Table 3.4 .

The total absolute systematic error, for both pp and dAu data sets, are listed in Table 3.5.

3.2.5 Event Selection

The Zero Degree Calorimeters and the Beam-Beam Counters provide a minimum-bias trigger for d+Au and p+p collisions respectively. The d+Au trigger required an energy deposition of approximately 15 GeV in the ZDC from the Au direction, while the p+p minimum-bias trigger required a coincidence of the two BBCs.

centrality	uncorrected FTPC East multiplicity	impact parameter (b)	N_{part}	N_{coll}
minbias (0-100%)		5.75	8.31	7.51
central(0-20%)	$N_{FTPC-E} \geq 17$	3.42	15.69	15.07
middle (20-40%)	$10 \leq N_{FTPC-E} < 17$	4.57	11.17	10.61
peripheral (40-100%)	$0 \leq N_{FTPC-E} < 10$	6.83	5.14	4.21

Table 3.6: The dAu centrality definitions and the impact parameter, number of binary collisions and number of participants calculated with the Glauber model.

Because the interacting particle beams cross each other at very small angles, the collision vertex distribution is broad along the beam axis. This observation, combined with the fact that the event reconstruction efficiency is strongly dependent on the vertex position, lead to the necessity of a cut on the vertex position to ensure uniform detection performance. Primary vertices within ± 50 cm of the center of the TPC along the beam line were selected.

dAu data analysis was performed as a function of collision centrality. We expect that the most peripheral dAu interactions should be similar to the p+p interactions, with a small collision volume, and few re-interactions. The entire data set is divided in 3 centrality classes based on the measured charged particle multiplicity in the forward TPC (FTPC). These classes consist of 0-20%, 20-40% and 40-100% of the hadronic cross section. We present in Table 3.6 the multiplicity criteria for the centrality selection, together with the values for the $N_{part}, N_{collision}$ and impact parameter b calculated within the Glauber Model.

Results

We measured charged kaons at midrapidity in p+p and d+Au collisions at $\sqrt{s_{NN}} = 200$ GeV, over a wider p_T range than any of the traditional identification methods can reach. We present in this chapter the spectra for minbias p+p and d+Au data as well as the $0 - 20\%, 20 - 40\%$ and $40 - 100\%$ d+Au centrality bins. We show the yields and the $\langle p_T \rangle$ values obtained and construct the nuclear modification factors R_{dA} and R_{CP}. A detailed discussion of these results follows in the next chapter.

4.1   Spectra
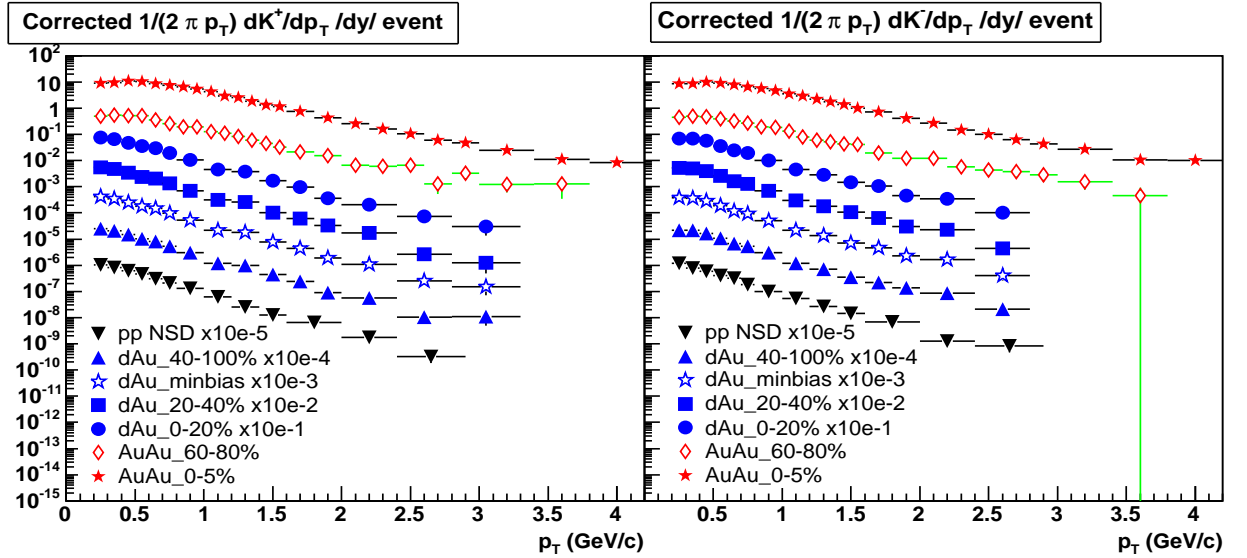
Figure 4.1: Corrected spectra for p+p, d+Au and (for completeness) Au+Au. For clarity, spectra are scaled with factors shown on the figure.

The corrected spectra $(1/2\pi p_T \times d^2N/dy/dp_T)$ per event, for midrapidity ($|y| <$
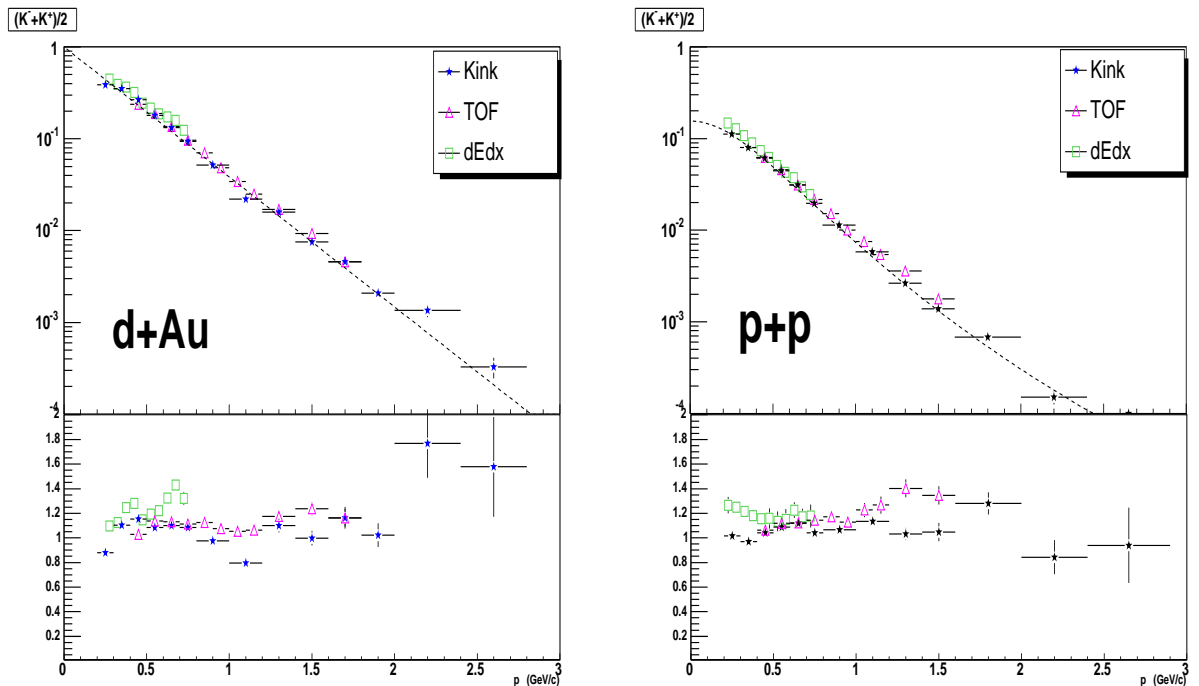
Figure 4.2: Kaon spectra comparison. The results are from 3 different STAR charged kaons analysis: kink, dE/dx and TOF. In the lower panels, all spectra are divided by one common curve (black dashed line in the upper panel) for making easier to observe the difference between different analysis.

0.5) p+p (NSD) and d+Au collisions at $\sqrt{s_{NN}} = 200\,\mathrm{GeV}$, for both positively and negatively charged kaons, topologically reconstructed in the Time Projection Chamber of STAR, are presented in Figure 4.1. For completeness and comparison, the spectra from central 0-5% and peripheral 60-80% Au+Au collisions ([65]) are also shown. For clarity, the spectra are scaled with the factors on the figures.

For consistency, we show in Figure 4.2 a comparison between the result of this analysis and two other STAR charged kaon analysis, from dE/dx and TOF. If we plot the ratio of each analysis to a common curve (lower panels), we can conclude that all four results are consistent within 20% for $p_T > 1\,\mathrm{GeV/c}$ for both pp and dAu data sets.
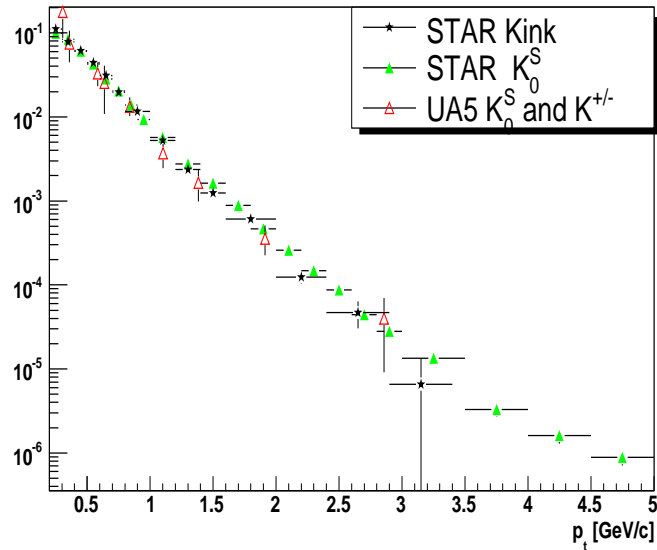
Figure 4.3: Kaon spectra comparison: STAR p+p and UA5 p + $\overline{\mathrm{p}}$.

Outside RHIC, the only measurement of kaons at $\sqrt{s_{NN}} = 200 \,\mathrm{GeV}$ is the one performed for p $+\overline{p}$ by the UA5 Collaboration [63] in the pseudorapidity range $|\eta| < 2.5$. At mid-rapidity, we do not expect any differences between p+p and p $+\overline{p}$ since we are far from beam rapidity. There are three UA5 points for charged kaons and the rest are for neutral kaons. After using HIJING to correct for the different acceptance and measured cross section between STAR and UA5 [64], we plot the charged kaons and the K_S^0 STAR results, together with the UA5 results in Figure 4.3. We can say that after applying all the corrections, the p_T spectra are consistent between the two experiments.

We have shown in this first chapter on results that the output of this analysis is consistent within and outside RHIC analysis.

Ratio	p+p minbias	d+Au minbias	dAu central 0-20 %	dAu mid-central 20-40 %	dAu peripheral 40-100 %
K^-/K^+	0.926±0.015	0.958±0.014	0.965±0.015	0.960±0.015	0.949±0.015

Table 4.1: K^-/K^+ for p+p NSD minbias and d+Au minbias, 0-20%, 20-40% and 40-100%.

4.1.1 K^-/K^+

In Figure 4.4 we plot the ratio of negative to positive charged kaons for p+p, d+Au obtained with this analysis, and we plot for comparison the Au+Au results for central (0-5%) and peripheral (60-80%) collisions.

The results reveal, for the momentum range achieved in this analysis, within errors, a flat K^-/K^+ ratio as a function of p_T and a constant integrated value in all three systems studied, as expected at mid-rapidity. Integrated values are shown in Table 4.1.

Figure 4.4: K^-/K^+ for p+p minbias (NSD), d+Au (0-20%, 20-40%, 40-100 %) and Au+Au (0-5%)

4.2 Soft p_T

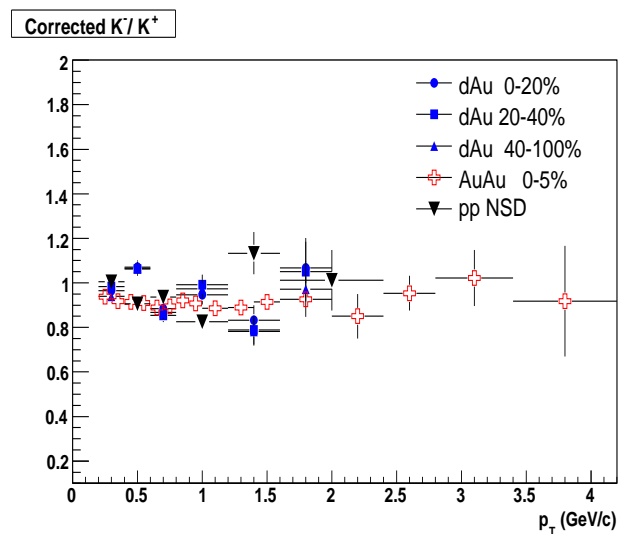One way to characterize the change in spectra as a function of system size is to calculate the $\langle p_T \rangle$ for each spectrum. Using the fit function method described in Chapter 3, we calculated the $\langle p_T \rangle$ and yield $\langle dN/dy \rangle$ values for both K^- and K^+. The results are listed in Tables 4.2 and 4.3 . The systematic errors for these measurements are calculated by varying the fit functions, the cuts, and using different methods for background subtraction (for details see Section 3.2.4) .

$\langle dN/dy \rangle$	K^+	K^-
p+p NSD	$0.142 \pm 0.001 \pm 0.006$	$0.137 \pm 0.001 \pm 0.009$
d+Au $0-100\%$	$0.595 \pm 0.001 \pm 0.018$	$0.592 \pm 0.003 \pm 0.038$
d+Au $0-20\%$	$1.163 \pm 0.002 \pm 0.018$	$1.168 \pm 0.004 \pm 0.038$
d+Au $20-40\%$	$0.816 \pm 0.008 \pm 0.018$	$0.816 \pm 0.008 \pm 0.038$
d+Au $40-100\%$	$0.346 \pm 0.001 \pm 0.018$	$0.340 \pm 0.001 \pm 0.038$

Table 4.2: $\langle dN/dy \rangle$ values for p+p and d+Au. Both statistical and systematical errors are shown in the format $x \pm \Delta x_{statistic} \pm \Delta x_{systematic}$.

$\langle p_T \rangle$	K^+	K^-
p+p NSD	$0.602 \pm 0.019 \pm 0.015$	$0.584 \pm 0.002 \pm 0.012$
d+Au $0-100\%$	$0.637 \pm 0.018 \pm 0.020$	$0.668 \pm 0.008 \pm 0.024$
d+Au $0-20\%$	$0.658 \pm 0.007 \pm 0.020$	$0.691 \pm 0.004 \pm 0.024$
d+Au $20-40\%$	$0.635 \pm 0.045 \pm 0.020$	$0.650 \pm 0.027 \pm 0.024$
d+Au $40-100\%$	$0.609 \pm 0.012 \pm 0.020$	$0.651 \pm 0.005 \pm 0.024$

Table 4.3: $\langle p_T \rangle$ values for p+p and d+Au. Both statistical and systematical errors are shown in the format $x \pm \Delta x_{statistic} \pm \Delta x_{systematic}$.

4.2.1 $\langle p_T \rangle$ and $\langle dN/dy \rangle$

Figure 4.5 presents the charged kaon $\langle p_T \rangle$ values from p+p and d+Au collisions versus N_{part}, obtained using the present analysis. For comparison, the results from TOF (obtained by averaging results obtained using a power law and an exponential fit function) and dE/dx analysis (results from an exponential fit function) are also
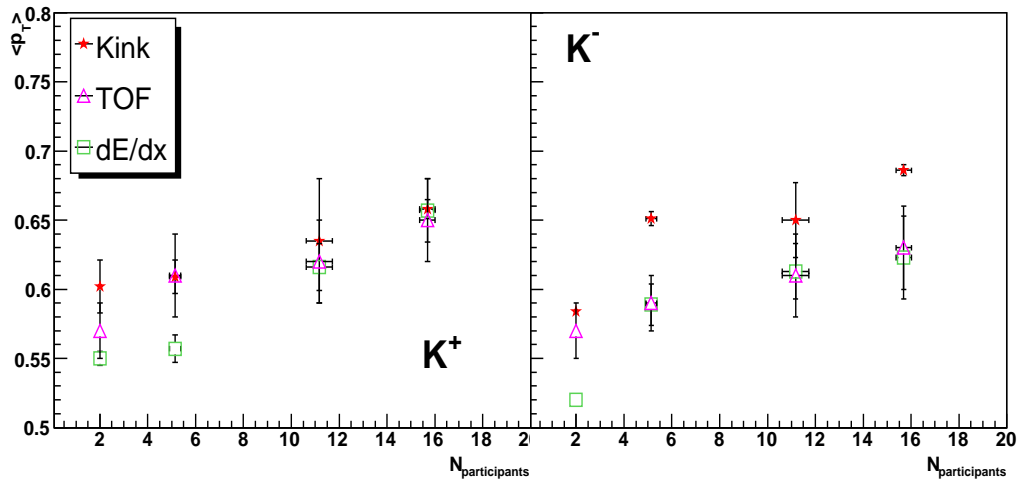
Figure 4.5: $\langle p_T \rangle$ from p+p to central d+Au versus N_{part}.

shown. Our pp result for $(K^- + K^+)/2$ is consistent also with the UA1 reported result, 0.44, for K_S^0.

The obtained charged kaon yields are presented in Figure 4.6 versus N_{part}. An
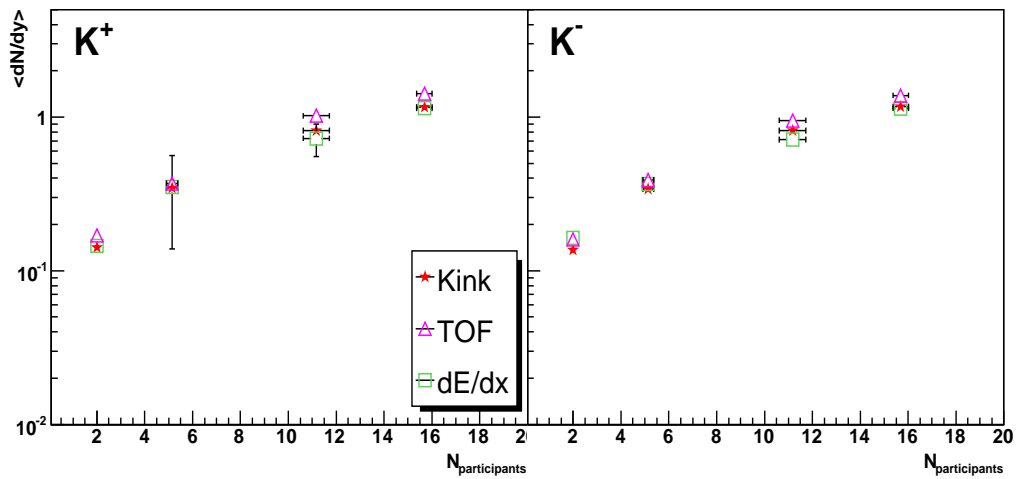
Figure 4.6: $\langle dN/dy \rangle$ from p+p to central d+Au versus N_{part}.

increase in yield is observed going from p+p to d+Au peripheral to d+Au central collisions. The errors for the kink kaons in both these plots are statistical only.

4.3 Intermediate and high p_T

4.3.1 Nuclear Modification Factors

Figure 4.7 shows R_{AA} and R_{dA} in which the yields ratio of minbias d+Au/central Au+Au to p+p minbias data was made. The p+p data are scaled to the number of binary collisions N_{binary} in order to account for trivial geometric effects. In Figure 4.8, we present the yield ratio of central to peripheral collisions R_{CP}. In both figures, the expectations for binary(N_{binary}) and participant (N_{part}) scaling are represented by the bands, where the errors coming from the model calculation were taken into account when representing the widths of the bands.

R_{CP} for dAu is consistent with binary scaling within errors while R_{dA}, in the p_T range reached, presents little enhancement. The difference between positive and negative kaons is not very significant statistically. However, the R_{dA} and R_{CP}^{dA} are clearly different in features to the corresponding Au+Au ratios: the d+Au nuclear modification factors are enhanced while the Au+Au nuclear modification factors are suppressed at all p_T, compared to binary scaling. Compared to participant scaling, R_{AA} increases up to $p_T \simeq 1.5\,\mathrm{GeV/c}$ where its maximum of 0.6 is reached, and then it falls again at higher p_T. These two figures are also an illustration of the advantages of using R_{CP}, where data for the same system are used for both nominator and denominator, instead of R_{AB}, where data from two distinct collision systems are used in the denominator and numerator. The statistical error bars are smaller for the R_{CP} plots, and the p_T coverage higher.
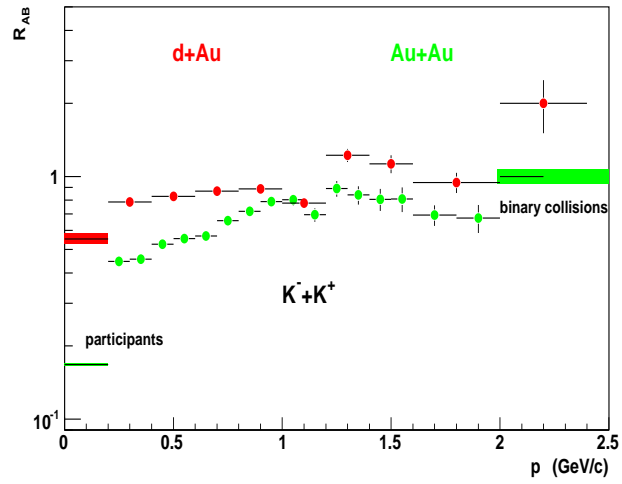
Figure 4.7: R_{AA} and R_{dA} for charged kaons.
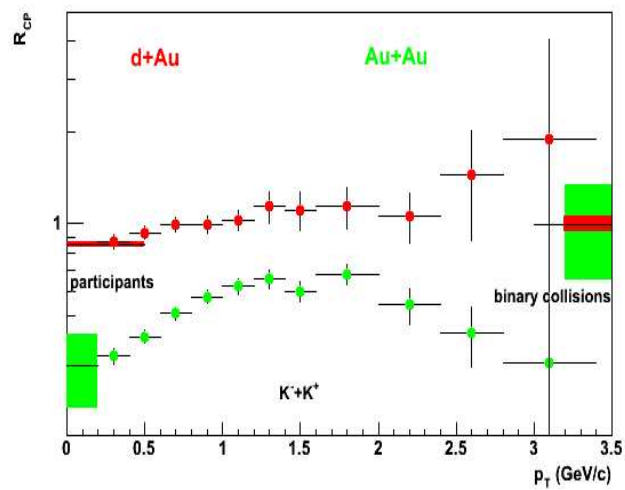
Figure 4.8: R_{CP} for charged kaons in d+Au and Au+Au.

Chapter 5

Experimental Results and Theoretical Interpretations

5.1   Introduction

Inclusive hadron studies of central to peripheral ratios (R_{CP}) and central to p+p
ratios (R_{AA}), reveal (after scaling factors are taken into consideration to account for
the different nuclear geometry) suppression in central Au + Au collisions [31]. The
most popular explanation for this effect is that a highly energetic parton moving
through a dense colored and deconfined medium loses energy due to collisions and
induced gluon radiation, so that its final fragmentation gives rise to particles with
considerably lower energy.   However the final measurement is influenced not only
by the produced medium, via energy loss or interactions, but also by initial state
effects (e.g. multiple scattering, gluon saturation, energy loss in cold nuclear matter,
etc). A baseline comparison was therefore needed to disentangle the final state effects
from the initial state effects. This was the purpose of the d+Au collisions at RHIC
and the results (both ratios presented a lack of suppression [32, 33]) provided a
critical cross-check that the quenching observed in Au+Au is not entirely an initial-
state effect but rather a final state effect. Models assuming fragmentation as the
hadronization mechanism and taking into account initial states effects (initial k_T
broadening, modification of the parton distribution functions) and final states effects
(energy loss) reproduce the shape and magnitude of the suppression ([72], [73], [74],
[75], [76]).

However, the analysis of identified hadrons brought new features to the R_{CP} picture:
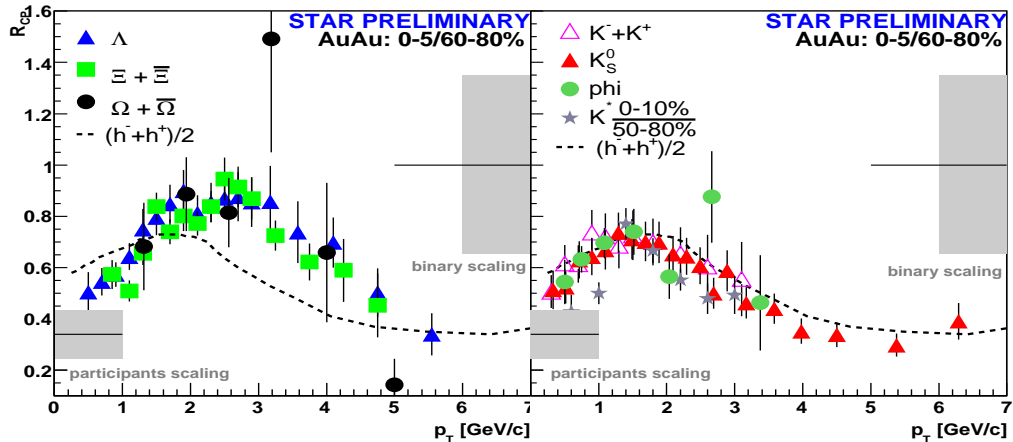
Figure 5.1: R_{CP} for identified hadrons.

mesons and barons were suppressed differently in the intermediate p_T region between 2.5 and $6\,\mathrm{GeV/c}$, the effect being species dependent and not just a mass effect, since the heavy mesons, ϕ and K_0^*, follow the curve for lighter mesons ([35] and Figure 5.1). Coalescence models provide a qualitative explanation (see [37]): the baryons need three quarks to coalesce while mesons require only two, and this pushes the baryon suppression to higher p_T.

So, the study of nuclear modification factors for **unidentified charged hadrons** sketched the properties of the nuclear medium created during RHIC collisions and delimited the physics regime into 'low' and 'high' p_T. The R_{CP} of **identified hadrons** studies provided insight into the hadronization mechanisms and made natural the splitting of the 'physics' scale at RHIC in 'low', 'intermediate' and 'high' p_T.

We present and discuss in the following the identified hadron measurements of R_{AA} and R_{dA}, measurements which were expected to confirm all the R_{CP} observations, similar to the results for unidentified particles. We discuss the implications of the analysis in terms of hadronization mechanisms, theoretical models being invoked to

help understand the features present in the data.

5.2 R_{dA}

In $\sqrt{s} = 38.8$, $27.4 \, \text{GeV}$ p+A collisions (where A = Be(9.01), W(183.85) [67, 69]), the cross section at a given p_T scales with $A^{\alpha(p_T)}$, with the power $\alpha(p_T) > 1$ for $2 \lesssim p_T \lesssim 5 \, \text{GeV/c}$ [67]. This was surprising, as the expectation for a 'hard' collision was that only one nucleon in the nucleus would be involved in the collision. Instead, the result implies that more than one nucleon is participating. Translated in terms of nuclear modification factors, this meant that there was an enhancement in the ratio at higher values of transverse momentum [69] (an experimental observation called Cronin effect). Furthermore, it was observed that there were also differences between particle types (bigger nuclear modification factors for kaons than for pions and bigger for protons than for kaons) and more than this, differences between particles and antiparticles. The enhancement was thought to be due to the multiple scattering of the incident partons while traversing the nucleus A, before the hard scattering took place [70]. The antiparticle-particle difference has been understood as a dominance of valence quarks in particles (e.g. K^+), and of gluons in antiparticle, (K^-), since the gluons have larger broadening of k_T (due to intense multiple scattering).

We present in this section the nuclear modification factor measured in the STAR experiment for d+Au collisions at $\sqrt{s} = 200 \, \text{GeV}$. The baryons (protons,$\Lambda$, Ξ) are on the left panel while the mesons (kaons and pions) are on the right side. The dashed lines represent the charged hadrons measurements, the same as presented in Chapter 1, in Figure 1.1 . The Cronin Effect is present for both mesons and baryons, but a difference is also evident. The statistics available (mostly from p+p collision) did not allow us to perform a separate analysis for particles and antiparticles. However
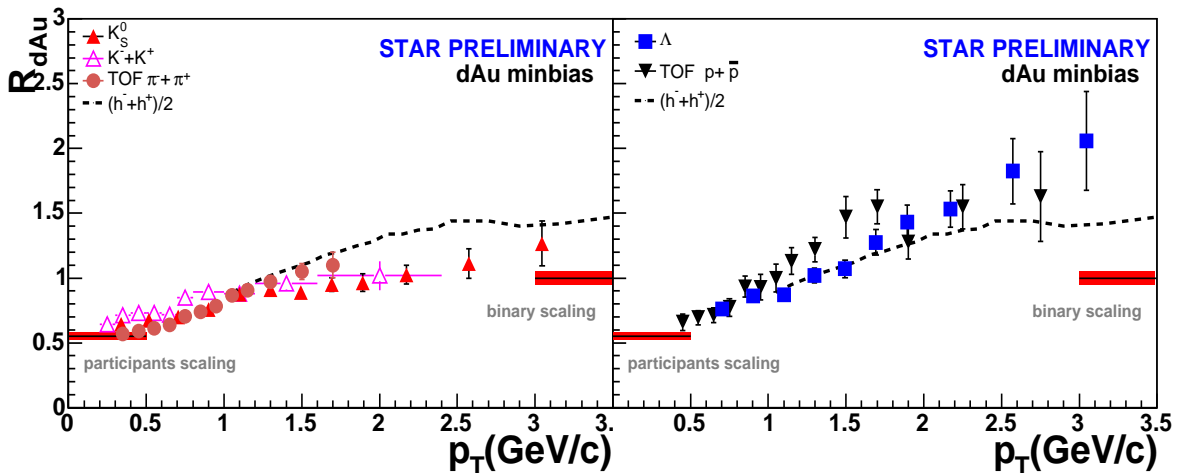
Figure 5.2: R_{dA} for identified hadrons.

gluons dominate at RHIC and hence, particles and antiparticles are almost equally produced (and we've seen this in the previous chapter in the ratio plot). Therefore, we expect the nuclear modification factors to be the same unless p_T is so large that valence quarks become important. The unimportance of valence quarks in the p_T range studied, can be demonstrated by plotting R_{CP} in d+Au for both K^+ and K^- (Figure 5.3), where we can see that within statistical errors, the two ratios overlap in the p_T region covered.

5.2.1 Initial state effects

The majority of theoretical models, with one exception that we discuss in the next paragraph, treat the Cronin effect at RHIC in terms of initial multiple interactions [72, 73, 74, 75, 76]. They differ in the object which is undergoing rescattering (the projectile hadron or its partons) and in the hardness of the assumed rescattering process. The theoretical calculations of Kopeliovich et al [74] for pions are shown
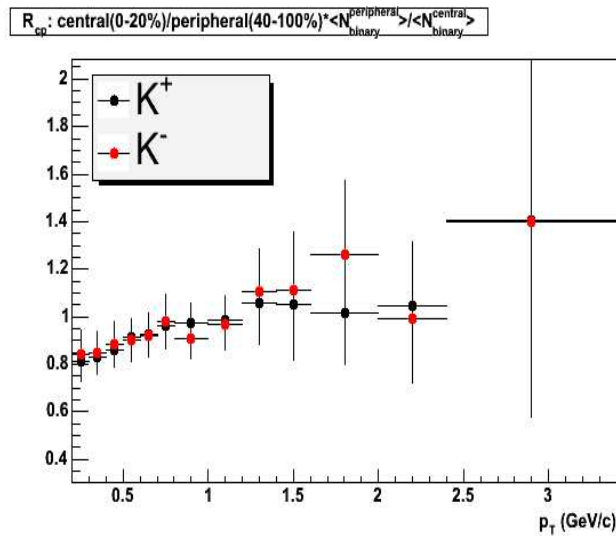
Figure 5.3: R_{CP} for K^- and K^+ separately.

in Figure 5.4 superimposed on the STAR data. The curve does not reproduce the meson-baryon difference present in the experimental data, but it does follow the curve for the mesons. The mechanism which produces the species-dependence of R_{dA} (in
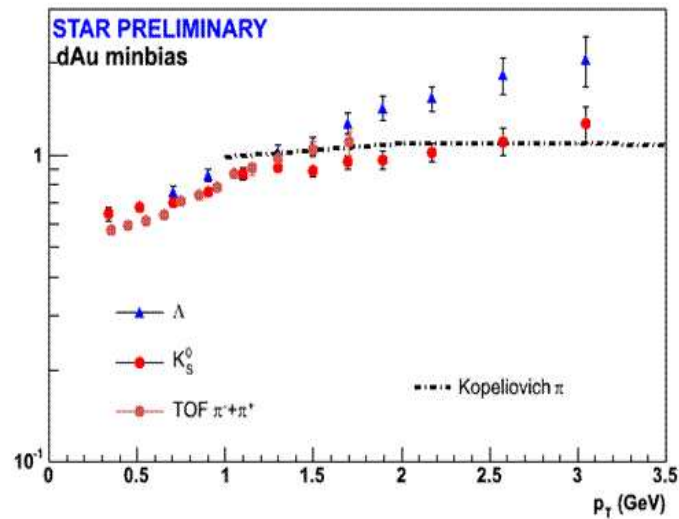
Figure 5.4: R_{dA} with theoretical calculations from [74].

the view of Kopeliovich et al), though not technically implemented yet, is understood in terms of different gluon fragmentation scenarios for the two cases. Gluons

are assumed to produce string junctions which become baryons after string breaking. Junctions take almost maximal fraction $z \sim 1$ of the gluon momentum, while mesons are mostly produced with small z. Since the p_T of the hadron is equal to k_T of the parent gluon times z, this can explain why baryons have larger p_T broadening and stronger Cronin effect.

A hint for the presence of the Cronin effect (and also a possible supporting argument for the presence of multiple scatterings in the initial phase of the collision) can be seen by plotting the $\langle p_T \rangle$ values as a function of the mean number of participants in the collisions (from p+p up to the most central Au+Au) in Figure 5.5. The 'jump' observed when passing from d+Au to peripheral Au+Au might be a signature of the Cronin enhancement: the spectra are softer, because the small p_T particles were pushed to higher p_T by initial multiple scattering. However, most interestingly,the
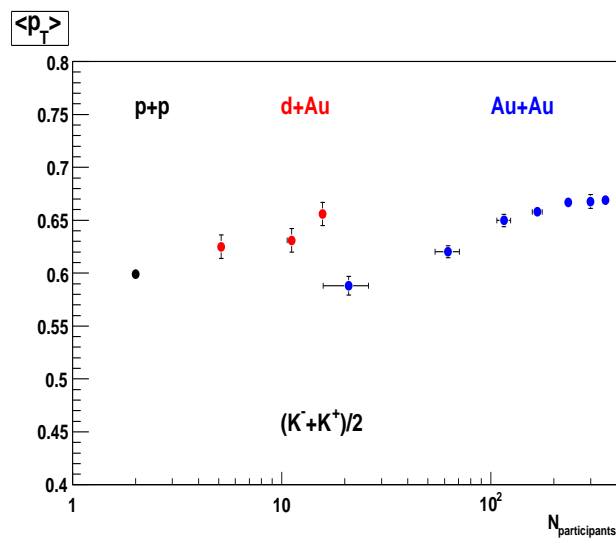

Figure 5.5: $< p_T >$ from p+p, d+Au and Au+Au versus N_{part}.

HERMES experiment revealed the presence of the Cronin Effect in $\sqrt{s} = 7.3\,\mathrm{GeV}$ Deep Inelastic Scattering (DIS) reactions with positron beams at the DESY laboratory. The results are presented in Figure 5.6 in terms of the hadron multiplicity
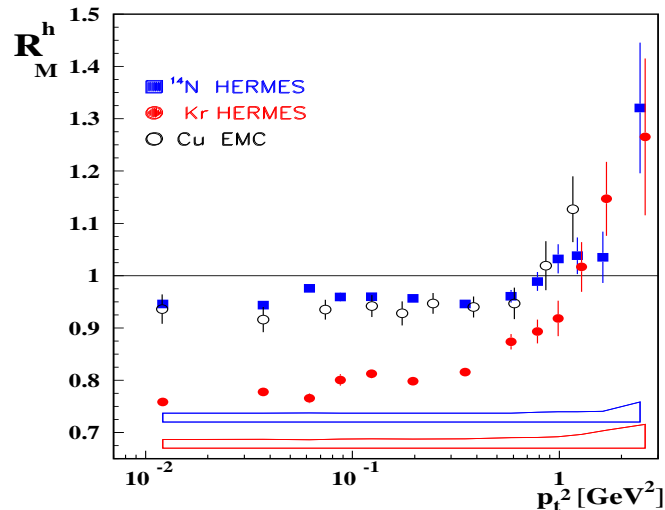
Figure 5.6: DIS data from HERMES. R_M^h vs p_T^2 for charged hadrons for $\nu > 7$ (the energy in the target rest frame) and $z > 0.2$ (the parton energy fraction carried by the hadron) at $\sqrt{s} = 7.3\,\text{GeV}$. The band represents the systematic uncertainty [71].

ratio R_M^h, which represents the ratio of the number of hadrons of type h produced per deep-inelastic scattering event in a nuclear target of mass A, to that from a deuterium target (D). The initial (i.e pre-hard scattering) interactions which boost the momentum at higher p_T can't be invoked here, because the initial interaction between the electron (positron) takes place via the exchange of a virtual photon with one of the quarks in the nucleons. We are led to conclude that final state effects (hadronic or partonic interactions) are responsible for the HERMES results.

5.2.2   Final state effects

The parton coalescence concept was applied by a theory group also to the d+Au collision system [77]. They found that *final state* hadronization mechanism produces the features seen in R_{dA}, namely, the difference between meson and baryons and the Cronin enhancement (see Figure 5.7). A first objection to this kind of treatment would be that such an enhancement was observed also in Drell-Yan processes [78]
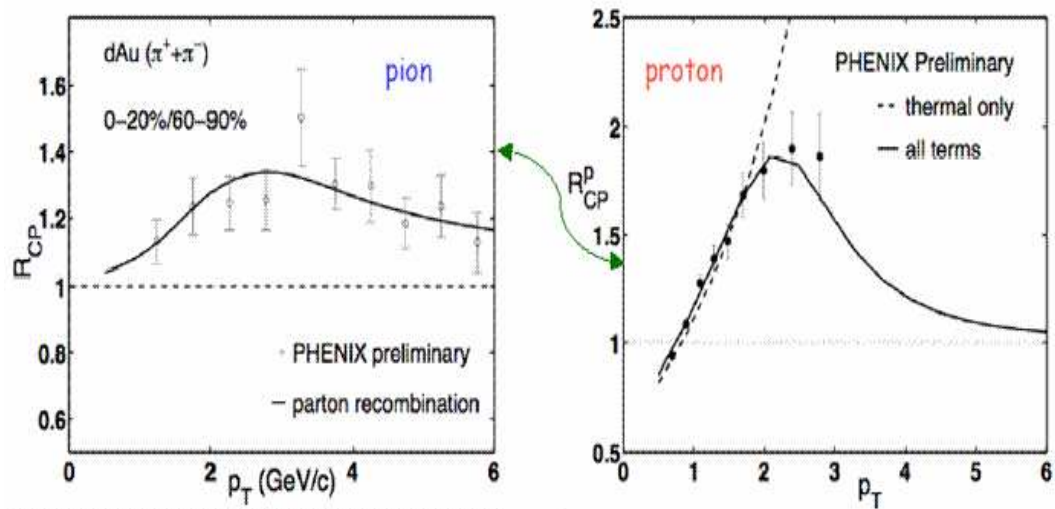
Figure 5.7: R_{CP} from recombination model [77] for protons and pions for PHENIX results.

in 800 MeV proton beams on different targets by experiment E772 at Fermilab (Figure 5.8). There is no 'final medium' for the di-muon pairs and hence the recombination explanation would not hold. However, if we accept the working definition we
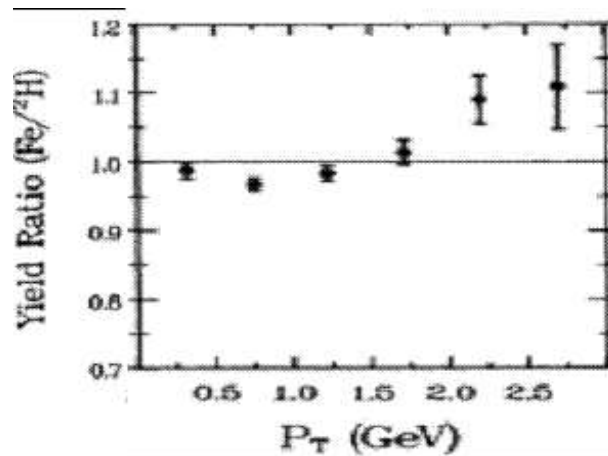
Figure 5.8: Drell-Yan production at Fermilab.

started with for the Cronin effect, that it is an *experimental observation*, which does not come with any intrinsic explanation, then we also accept that the enhancement
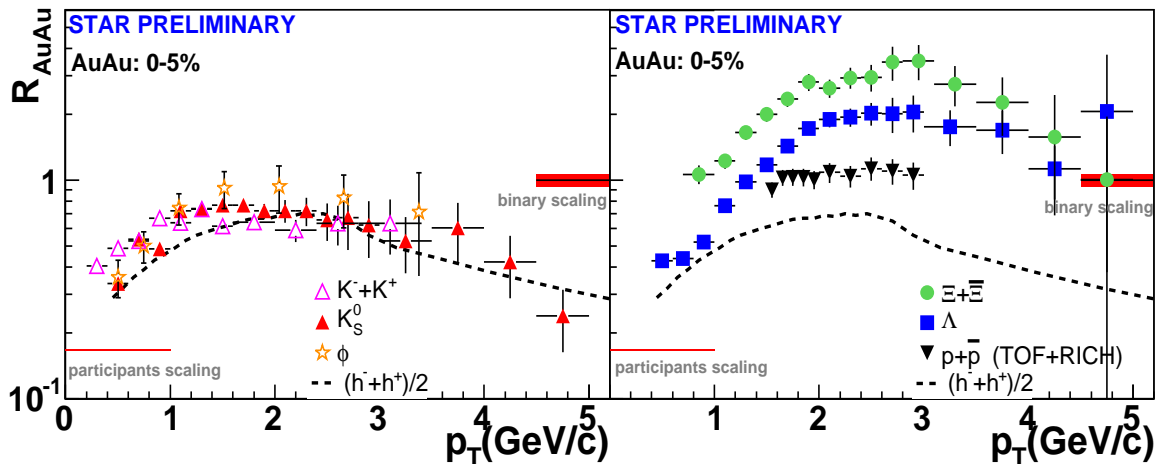
Figure 5.9: R_{AA} for identified hadrons.

observed at different collision energies for different observables can have different explanations: initial parton scattering (before hard-scattering stage) and/or final state recombination.

5.3 R_{AA}

In Figure 5.9, the R_{AA} for different baryons and mesons is presented as a function of p_T for central AuAu collisions. The R_{AA}^{meson} is rather consistent with the R_{CP}^{meson}, the same as for the non-strange baryons (protons) [66]. However, for the strange and multi-strange baryons, the R_{AA}^{baryon} shows the opposite effect to the published R_{CP}^{baryon} results [36]: it is not reduced but increased compared to binary scaling in the intermediate (2 to 6 GeV/c) p_T region. Moreover, there seems to exist an ordering which follows the strange quark content: Ξ hyperons (strangeness $S = -2$) are enhanced more than Λ hyperons ($S = -1$) which are in turn enhanced more than protons ($S = 0$). While the experimental results on R_{CP} point to the validity of the quark coalescence picture, several other models found a different explanation to

describe both the central to peripheral ratio and the central to pp ratio [81, 80]. In particular, HIJING/B$\overline{B}v2$ [80] attributes the 'baryon anomaly' to the presence of an additional baryon production mechanism (string junctions and junction loops), which has an increasing contribution from pp to d+Au to Au+Au collisions (Figure 5.10). In the same string fragmentation scenario, the presence of 'strong color field' effects influences the strange baryon production and produces the strangeness ordering in the R_{AA} plot.
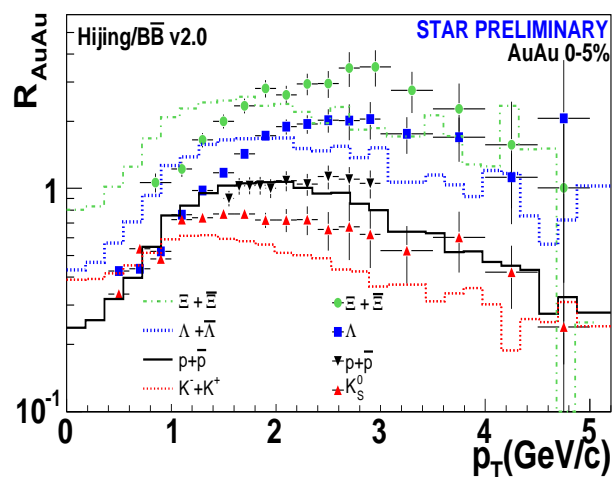
Figure 5.10: R_{AA} for identified hadrons. The markers are the experimental points while the curves the theoretical calculations from [80].

5.4 Canonical suppression

In addition to these hadronization scenarios, other effects might influence the d+Au and Au+Au to p+p spectra ratios. In particular, if canonical suppression[1] [82] dominates the strange baryon production in p+p collisions but not in peripheral

---

[1]In small (micro-canonical) systems, all quantum numbers have to be conserved explicitly. This implies that besides energy, there must be also phase space available for strangeness production. This leads to a suppression of strangeness production in small systems, due to the lack of available phase-space.
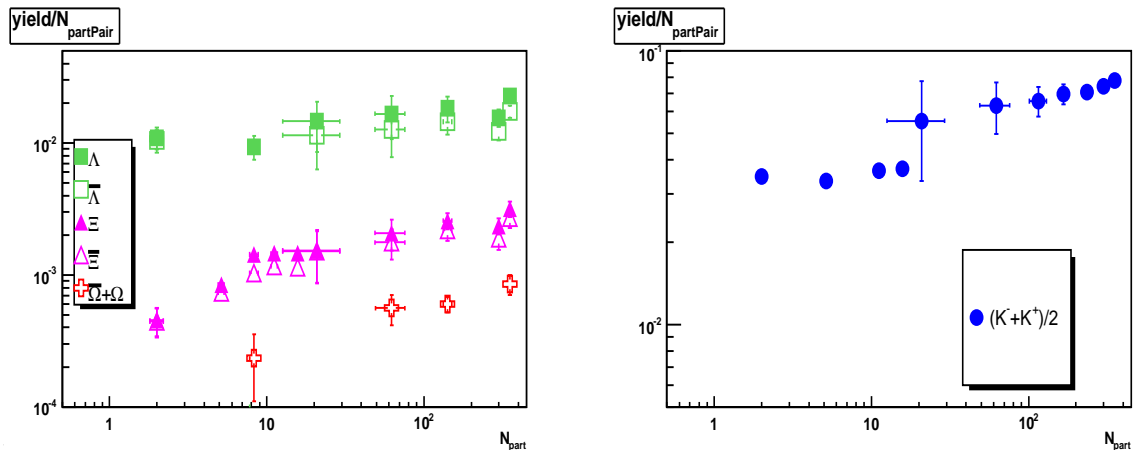
Figure 5.11: Yield per N_{part} vs N_{part} for p+p, d+Au and Au+Au.

Au+Au collisions, then a plausible reason for the R_{AA}^{baryon} increase with respect to binary scaling is not an enhancement of the yield in central Au+Au collisions, but a suppression of the yield in p+p collisions. It was shown that this suppression will increase as a function of strangeness content for baryons, and therefore it should lead to larger differences between R_{CP} and R_{AA} for multi-strange baryons than for singly strange or non-strange baryons.

Figure 5.11 presents the yield per participant pair versus N_{part}, separately for baryons and mesons at $\sqrt{s} = 200\,\text{GeV}$. Indeed, although the number of participants is not an accurate measure of the collision volume, we see a bigger difference when going from p+p to Au+Au for baryons than for mesons, and among the baryons the difference grows from strange to multi-strange baryons. We also note that although the ordering is clearly present in R_{AA}, there seems to be an ordering also in d+Au collisions but *reversed*. We sustain our phase-space suppression idea, by plotting the R_{dA} numbers with the Ξ values added in Figure 5.12. If this is confirmed, it would be a really interesting phenomenon: it would mean that the strange baryons see different
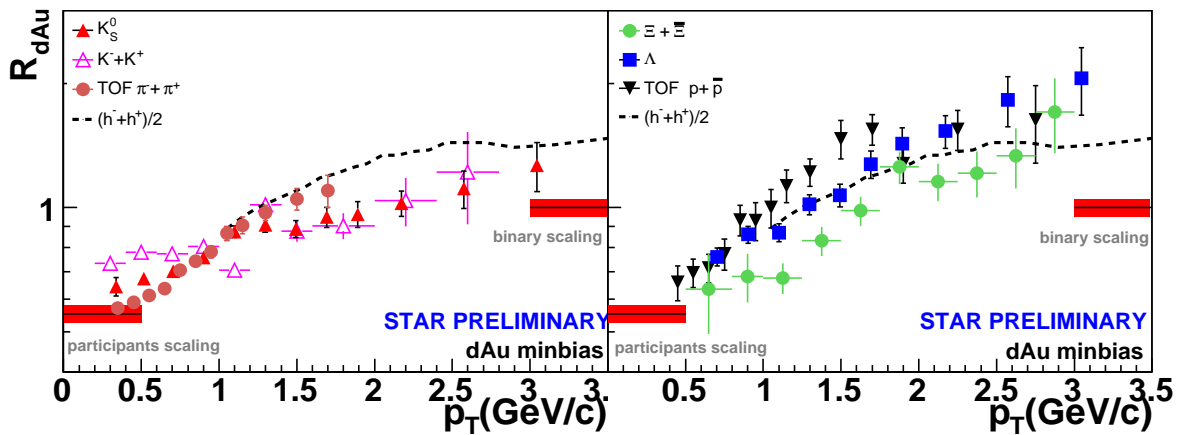
Figure 5.12: R_{dA} for identified hadrons.

hadronization volumes because of the strange quark. It is clear that for baryons the ratio to p+p is different from the ratio to peripheral. However, mesons also show this phenomenon, but the difference is smaller [83].

5.5 A different nuclear modification factor

Another difference between elementary pp collisions and peripheral AuAu collisions is that initial state effects should be present in AuAu but not in pp collisions. Thus, R_{CP} contains information only about final state effects (assuming same initial state effects in peripheral and central collisions of AuAu) whereas R_{AA} ratios, sample both initial and final states effects. Although the effect of gluon saturation should not be particle specific, it is interesting to note that the gluon distribution changes in the initial system when comparing pp to peripheral AA collisions [79].

A better way of trying to eliminate the initial effects in the Au+Au analysis, is to take the ratio to d+Au collision instead of the ratio to p+p. If the assumption is that all the initial effects present in Au+Au are also present in d+Au, but none of

the final effects are present, then this should be a more accurate picture of the final suppression in central Au+Au.

Chapter 6

Conclusions and Future Directions

6.1   Conclusions

We present results for charged kaons topologically reconstructed in p+p and d+Au
collisions. These measurements, in combination with other identified particle mea-
surements, are important for understanding the properties of the medium created
in Au+Au collisions. Our kaon results confirm the prior results obtained with the
default particle ID methods and extend them much higher in p_T coverage.

The importance of our wide coverage in transverse momentum for identified particles
in three different systems is illustrated by analyzing nuclear modification factors. The
d+Au and Au+Au yields compared to $\langle N_{part} \rangle$-scaled pp yields helps to test not only
the assumption that a nucleus-nucleus collision is more than a simple superposition of
incoherent nucleon-nucleon scatterings, but also explores hadronization mechanisms
and nuclear effects. The Au+Au high-p_T suppression of the inclusive hadron yields
observed at RHIC is a unique phenomenon that has not been previously observed in
any hadronic or heavy-ion reaction at any energy. Novel phenomena appear when we
look at identified hadrons. We see differences between mesons and baryons, and be-
tween strange and non-strange baryons. The Au+Au yields of mesons are suppressed
but a significant enhancement is noticed for baryons and the enhancement increases
with the number of strange valence quarks in the baryon. At intermediate p_T, the
R_{AA} values are much higher than the binary scaling of p+p data would predict. The
fact that the effect is not present in R_{CP} ratios points to phase-space suppression

77

effects of baryons in p+p, which extend beyond the region where soft physics (below 1 GeV/c in transverse momentum) is expected to dominate. So we conclude that the measured R_{AA} displays the combined effects of strangeness enhancement and jet suppression, with the former dominating at intermediate p_T. We can affirm that these differences observed in Au+Au are present also in d+Au, but at a smaller level. Different hadronization mechanisms (quark recombination, string fragmentation) can qualitatively describe the data. Further measurements will be necessary for the establishment of a single theory to describe all the measurements.

6.2   Peek into the future

In the big picture, the next natural step in the future is to find the properties of the matter created in central Au+Au collisions at RHIC. What we know for sure at the present is that this new form of matter is highly interacting, and that quark and gluon degrees of freedom are necessary to describe the experimental results for which purely hadronic descriptions have failed. What this means is that the role of identified-particle studies has increased in importance, because it is exactly the role of these studies to make the transition from the discovery phase to the description phase of QGP.

High p_T particles and jets proved to be a useful tool in conducting collider physics studies and can still help illuminate the future in several directions. In jet and leading particle measurements, the fragmentation function of identified particles can (and will) be measured and compared to those measured in p+p interactions to determine precisely the modification of the fragmentation functions of specific particles as a function of their quark content and also the flavor dependence of hadronization. This is essential to ascertain the properties of the high density state and to understand the

interaction of this state with the traversing partons.

We made the first step in pursuing such jet-like study using charged kaons from kinks, inspired by previous results in e^+e^- collisions. Studies of correlations between identified charged hadrons produced in hadronic Z^0 decays were previously conducted to probe details of the jet fragmentation process ([84], [85]). In $e^+e^- \rightarrow Z^0 \rightarrow q\bar{q}$ annihilations, there must be conservation of total charge, strangeness, baryon number etc. These experiments looked to see whether the conservation is:

(i) local - a particle and its antiparticle are produced close to each other;

(ii)long range - the particle and its antiparticle are associated to the initial $q\bar{q}$ pair and hence separated from one another;

(iii) or random - particles and their antiparticles are randomly distributed.

The two collaborations cited above analyzed the distribution of the difference in rapidity of identified hadron pairs: $\Lambda, \overline{\Lambda}$ ([84]), pions, kaons, protons [85], using the same-sign and opposite-sign charges, and combinations between different particle species. The lambda-pair analysis showed short-range, local correlations which proved to be useful for testing and tuning fragmentation models, due to the necessity of compensating two quantum numbers: baryon number and strangeness. These data were used by the authors of JETSET [86] (where particle production proceeds through string fragmentation), JETSET/MOPS (which has the modified popcorn effect included) and HERWIG [87] (which describes fragmentation with clusters and their subsequent decay).

The same effect was observed when looking at charged hadrons, with an additional effect to account for the conservation of electrical charge. An excess of opposite-charged hadron pairs ($K^+K^-, \pi^+\pi^-, p\,\bar{p}, K^+\pi^-$, and all combinations) over pairs of like charge

$(K^+K^+, K^-\pi^-, \pi^-\overline{p}$, and all combinations) was reported at small absolute rapidity separations. In addition, a large excess of high-momentum K^+K^- pairs compared to same charge kaon pairs at large absolute rapidity differences was observed. This was attributed to the production of leading kaons in $s\overline{s}$ events, whereby higher-rapidity tracks in each jet tend to carry the quantum numbers of the initial quark or antiquark. In a $e^+e^- \rightarrow s\overline{s}$, the s and $\overline{s}$ quarks may hadronize into a high-momentum K^- and K^+, respectively, and there is no need for any other strange particle to be created. The effect was weaker for protons, an indication that leading baryons in di-jet events is not an important production mechanism for baryons in annihilation processes.

These results motivated a similar study using RHIC data from Au+Au collisions at $\sqrt{s_{NN}}$=200 GeV which could allow an insight into the particle production mechanisms in nuclear reactions. The characteristics of the STAR detector do not allow us to conduct a rapidity analysis similar to the ones described above. Nevertheless, we took advantage of the azimuthal symmetry and particle identification capabilities of the STAR detector and performed an azimuthal two-particle correlation study at mid-rapidity. Being statistics limited, we chose to study correlations of strange baryons $\Lambda, \overline{\Lambda}$ together with the strange mesons K^+, K^-. Our particle choice was motivated by quark content considerations. Our focus was on whether there is a correlation between $K^+(u\overline{s})$ and $\Lambda(uds)$ or between $K^-(s\overline{u})$ and $\overline{\Lambda}(\overline{uds})$, which would imply an $s - \overline{s}$ correlation, and on whether it is stronger in the away side or in the near side. Unfortunately, the results were inconclusive due to insufficient statistics at present. However, we believe that further investigation in this direction, with the much larger samples from future RHIC runs for p+p, d+Au and Au+Au, will be successful.

Appendix A

Kinematics

A.1 N_{binary}, N_{part}, impact parameter

In Figure A.1 we schematically display the geometry of a heavy ion collision: two incoming nuclei, each with number A of nucleons and nuclear radius R, collide at an impact parameter b. We define for this geometry a few parameters:

$\mathbf{N}_{part}$: number of incoming nucleons in the overlap region (shaded area), that suffer at least one collision; in the case of Au+Au collisions, the maximum number of participants is 197×2=394!

$\mathbf{N}_{binary}$: number of inelastic nucleon-nucleon collision.

impact parameter (**b**) : the distance between the centers of the colliding ions. It is used as a measure of the centrality of the system; the smaller the impact parameter, the more central is the collision.
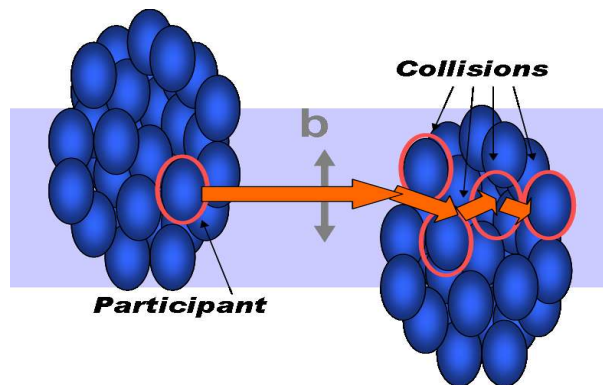

Figure A.1: Heavy ions collision geometry

We prove in the following two ubiquitous statements (intuitively easy to understand but rarely actually proven): the number of participants in the collision (N_{part}) acts as a measure of the size of the system (or more often seen in the form that $N_{part} \sim R^4 \sim A^{4/3}$ which has the dimension of area squared) while the number of collisions (N_{binary}) measures the longitudinal thickness of the system (or otherwise is said to be proportional to $R^{1/3}$) [88].

We consider first a nucleus with mass number A, for which the nuclear density $n_A(r)$ (the number of nucleons per unit volume) is given in the most simplistic case by

$$(A.1) \qquad n_A(r) = \begin{cases} n_0 & r \leq R \\ 0 & r > R \end{cases}$$

where n_0 is a constant and R is the nuclear radius, given by $R = (3A/(4\pi n_0))^{1/3}$. The density is normalized so that $\int d^3 r n_A(r) = A$.

The *thickness function* is the density integrated along the beam axis direction (z):

$$(A.2) \qquad T_A(b) = \int n_A(\sqrt{b^2 + z^2}) dz$$

which for our choice of the density distribution is

$$(A.3) \qquad T_A(b) = 2n_0\sqrt{R^2 - b^2} \rightarrow 2n_0 R \propto A^{1/3} \qquad b \rightarrow 0$$

If σ_{NN} is the notation for the total inelastic nucleon-nucleon cross-section, then the number of binary nucleon-nucleon collisions suffered by a nucleon passing through a nucleus at impact parameter b is

$$(A.4) \qquad N_{binary} = T_A(b)\sigma_{NN} \propto R \propto A^{1/3}.$$

Having established this, we look at the collision of the nucleus A with the nucleus B. For a given impact parameter $\vec{b} = \vec{r_A} - \vec{r_B}$, the overlap function is defined as the

thickness functions of the 2 nuclei, integrated over the two directions transverse to the beam directions:

$$(A.5) \qquad T_{AB}(b) = \int T_A(\vec{s}) T_B(\vec{s} - \vec{b}) d^2 s$$

By solving the 4-dimensional integral using our nuclear density, we obtain that for $b \to 0$ and A+A collisions, $T_{AA}(b) \to 2\pi n_0^2 R^4$.

$T_{AB} \sigma_{NN}$ is the N_{binary} in A+B collision at impact parameter b. Now, as we said, N_{part} is the number of nucleons that suffer at least one collision. The probability p_A for a nucleon to pass without suffering any collision is (using the binomial distribution of number of binary collisions)

$$(A.6) \qquad p_A(\text{ncoll} = 0) = (1 - \frac{\sigma_{NN} T_A(b)}{A})^A.$$

The N_{part} is then

$$(A.7) \qquad N_{part} = \int d^s T_A(\vec{s})[1 - p_B] + \int d^s T_B(\vec{s})[1 - p_A] \propto R^{1/3}.$$

A.2   Flow

We mentioned several times in this dissertation the term 'flow', meaning, if not specified otherwise, elliptic flow. The concept is schematically illustrated in Figure A.2. In a non-central heavy-ion collision, the spatial anistotropy (the 'almond' like shape of the reaction region in the transverse plane), causes azimuthal anisotropy in momentum space, which is correlated with the reaction plane (the plane defined by the beam direction and impact parameter). Elliptic flow is characterized by the second harmonic coefficient v_2 of the Fourier decomposition of the particle distribution:

$$(A.8) \qquad E\frac{d^3 N}{dp^3} = \frac{1}{2\pi}\frac{d^2 N}{p_T dp_T dy}(1 + \sum_{n=1}^{\infty} 2 v_n \cos n\phi)$$
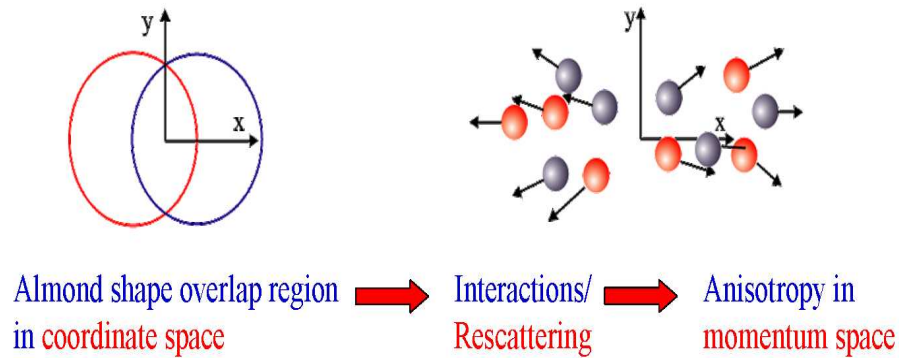
Figure A.2: Elliptic flow concept

where ϕ is the azimuthal emission angle, measured with respect to the reaction plane. A short calculation proves that, in general, the Fourier coefficients in Equation A.8 are given by the simple relation $v_n = \langle \cos n\phi \rangle$.

Because with time, the interactions cause the spatial distribution to be more isotropic, the final azimuthal momentum space anisotropy becomes established early in the system evolution. [89].

A.3 Two-particle azimuthal correlations

Important physics results can be derived from measuring the two-particle azimuthal correlations. We summarize in Figure A.3 the concept, the geometric picture and the actual measurement. We use the following terminology:

jet (blue and red arrows) a cluster of particles in phase space, which have in common that they all have been generated from the same primordial parton-parton scattering.

trigger particle (red arrows): the highest-p_T particle in a jet.

associated particles (blue arrows): particles connected via space proximity (same side) or opposite (back side) relative to the trigger particle, which also pass certain momentum cuts (cuts often correlated to the trigger momentum). The measurement
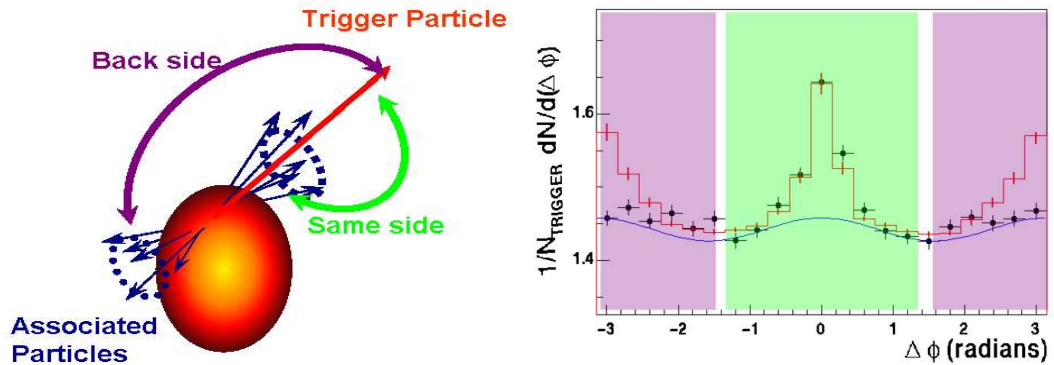
Figure A.3: Two particle correlation geometry dictionary

is as follows: there are selected events containing at least one particle which passes the trigger cuts (eg $p_T > 4 GeV/c, |\eta| < 0.5$, etc) which is designated the *trigger* particle. Then, for the same event we counted all hadrons, the *associated* particles, which pass the imposed particle cuts (eg $1.5 \leq p_T \leq p_T^{trig}$) as a function of their azimuthal separation ($\Delta\phi$) from the trigger particle .

The actual correlation function, $D(\Delta\phi)$, which represents the overall trigger-associated particle pair distribution per trigger particle is defined as

$$(A.9) \qquad D(\Delta\phi) = \frac{1}{N_{trigger}} \sum N_{pairs}(trigger, associated)(\Delta\phi)$$

where $N_{trigger}$ is the number of trigger particles which passed the trigger cuts.

$D(\Delta\phi)$ is plotted in the right side of Figure A.3, with the *same side* and the *back side* highlighted in pink and green respectively.

One of the main sources of background that we have to account for are correlations generated by the elliptic flow of single particles relative to the reaction plane. The elliptic flow pushes in the same direction particles, which later can be interpreted as being part of the same jet, on account of proximity in space. The flow component is represented by the blue curve in the right plot in Figure A.3.

References

[1] J.C.Collins and M.J.Perry, Superdense Matter: Neutrons or Asymptotically Free Quarks? Phys.Rev.Lett. 34, 1353(1975)

[2] F.Karsch and E.Laermann, *Preprint* hep-lat/0305025

[3] Gyulassy M and McLerran L, *Preprint* nucl-th/0405013

[4] J.W.Harris and B.Müller The search for Quark-Gluon Plasma. Annu.Rev.Nucl.Part.Sci 46: 71-107 (1996)
B.Müller Physics and signatures of the quark-gluon plasma. Rep.Prog.Phys. 58: 611-636 (1995)
C.-Y.Wong Signatures of Quark-Gluon Plasma phase transition in high-energy nuclear collisions. *Preprint* nucl-th/0007146 (2000)
C.Greiner Signatures of Quark-Gluon Plasma: a personal overview. *Preprint* nucl-th/0012093 (2000)
E.L.Bratkovskaya et al. Review of QGP signatures-ideas versus observables. *Preprint* nucl-th/0401031 (2004)

[5] N.Herrmann et al. Collective flow in Heavy Ion Collisions Annu.Rev.Nucl.Part.Sci 49 581 (1999)

[6] T.Matsui and H.Satz Phys.Lett.B 178, 416 (1986)

[7] J.Rafelski and B.Müller Phys.Rev.Lett. 48: 1066 (1982)

[8] K.Kajantie et al. Dilepton emission and the QCD phase transition in ultrarelativistic nuclear collisions. Phys.Rev.D, 34, 2746 (1986)

[9] M.Gyulassy What have we learned at RHIC?, J.Phys.G:Nucl.Part.Phs. 30, 5911 (2004)

[10] I.G.Bearden et al (BRAHMS Collaboration) nucl-ex/0312023

[11] J.D.Björken, Phys.Rev.D 27, 140(1983)

[12] J.Adams et al (STAR Collaboration), Phys.Rev.C 70, 054907(2004)

[13] K.Adcox et al (PHENIX Collaboration), Nucl.Phys.A 757, 184(2005)

[14] X.N.Wang *Preprint* nucl-th/0307036

[15] P.F.Kolb and U.Heinz *Preprint* nucl-th/0305084

[16] P.F.Kolb and U.Heinz, *Preprint* nucl-th/0305084
P.Huovinen *Preprint* nucl-th/0305064

[17] C.Alt et al (NA49 Collaboration), Phys.Rev.C. 68, 034903 (2003)

[18] G.Agakichiev et al (CERES Collaboration), Phys.Rev.Lett. 92, 032301 (2004)

[19] D.A.Appel Jets as probe of quark-gluon plasma. Phys.Rev.D. 33, 717 (1986)
J.D.Björken Energy loss of energetic partons in Quark-Gluon Plasma: possible extinction of high p_T jets in hadron-hadron collisions. FERMILAB-Pub-82/59-THY (1982)

[20] X.W.Wang Hard Probes in high-energy heavy-ion collision. nucl-th/9711026

[21] J.C.Collins, D.E.Soper and G.Sterman Nucl.Phys.B 261, 104 (1985)

[22] J.F.Owens Rev.Mod.Phys. 59, 465(1987)

[23] X.-N.Wang Effects of jet quenching on high p_T hadron spectra in high-energy nuclear collisions Phys.Rev.C 58 (4), 2321 (1998)

[24] S.S.Adler et al (PHENIX Collaboration) Phys.Rev.Lett. 91, 241803 (2003)

[25] X.-N.Wang Systematic study of high p_T hadron spectra in pp, pA, and AA collisions at ultrarelativistic energies Phys.Rev.C 61, 064910 (2000)

[26] M.Gyulassy et al *Preprint* nucl-th/0302077

[27] J.Adams et al (STAR Colaboration) Phys.Rev.Lett. 91, 172302 (2003)

[28] K.Eskola, V.Kolhinen, C.Salgado Eur.Phys.J. C9 (1999)

[29] D.d'Enterria et al (PHENIX Collaboration), *Preprint*

[30] K.Gallmeister et al, Nucl.Phys.A 735, 277 (2004)

[31] J.Adams et al. (STAR Collaboration) Phys.Rev.Lett. 91 172302 (2003)
S.Adler et al. (PHENIX Collaboration) Phys.Rev.Lett. 88 022321 (2002)

[32] J.Adams et al, (STAR Collaboration) Phys.Rev.Lett. 91 072304 (2003)

[33] J.Adams et al, (STAR Collaboration)*Preprint* nucl-ex/0408016

[34] A.Accardi *Preprint* hep-ph/0212148

[35] J.Adams et al, (STAR Collaboration) Phys.Rev.Lett. 92 052302 (2004)

[36] K.Schweda (STAR Collaboration) Journal of Phys. G 30 693 (2004)

[37] R.J.Fries *Preprint* nucl-th/0403036

[38] J.Schaffner-Bielich What is so special about strangeness in hot matter? J.Phys.G. 30:R245 (2004)

[39] B.L.Combridge Associated production of heavy flavour states in pp and $p\bar{p}$ interactions: some QCD estimates. Nucl.Phys.B 151, 429 (1979)

[40] P. Koch et al. Strangeness in relativistic heavy ion collisions. Phys.Rpt. 142, 167-262 (1986)

[41] M.Harrison et al. RHIC Project Overview *Nucl. Instrum. Meth.*, A 499 (2003) 235-244

[42] M.Hahn et al. The RHIC Design Overview *Nucl. Instrum. Meth.*, A 499 (2003) 245-263

[43] M.Adamczyk et al. The BRAHMS experiment at RHIC *Nucl. Instrum. Meth.*, A 499 (2003) 437-438

[44] PHENIX Collaboration www.phenix.bnl.gov

[45] PHOBOS Collaboration www.phobos.bnl.gov

[46] K.H.Ackermann et al. STAR detector overview *Nucl. Instrum. Meth.*, A 499 (2003) 624-632

[47] K.H.Ackermann et al. The STAR trigger *Nucl. Instrum. Meth.*, A 499 (2003) 766-777

[48] STAR Collaboration http://www.star.bnl.gov/STAR/html/trg_l/

[49] F.Bergsma et al. The STAR detector magnet overview *Nucl. Instrum. Meth.*, A 499 (2003) 633-639

[50] M.Anderson et al. The STAR time projection chamber: a unique tool for studying high multiplicity events at RHIC *Nucl. Instrum. Meth.*, A 499 (2003) 659-678

[51] K.H.Ackermann et al. The forward time projection chamber in STAR *Nucl. Instrum. Meth.*, A 499 (2003) 713-719

[52] R.Bellwied et al. STAR detector overview *Nucl. Instrum. Meth.*, A 499 (2003) 640-651

[53] M.Beddo et al. The STAR Barrel Electromagnetic Detector *Nucl. Instrum. Meth.*, A 499 (2003) 725-739

[54] M.Harrison et al. The Relativistic Heavy Ion Collider Project: RHIC and its Detectors *Nucl. Instrum. Meth.*, A 499 (2003)

[55] W.Deng Charged Kaon Production in Au+Au collisions at $\sqrt{S_{NN}} = 130 GeV$ *Ph.D Thesis*, Kent State University (2002)

[56] GEANT Detector Description and Simulation Tool http://wwwasd.web.cern.ch/wwwasd/geant/

[57] M.Gyulassy, X.-N.Wang HIJING Monte Carlo Model http://www-nsdth.lbl.gov/ xnwang/hijing/index.html

[58] J.Adams et al (STAR Collaboration) *Inpreparation*.To be submitted to PRC

[59] H.Zhang K*(892) Resonance Production in Au+Au and p+p Collisions at $\sqrt{S_{NN}} = 200 GeV$ at the Relativistic Heavy Ion Collider *Ph.D Thesis*, Yale University (2003)

[60] P.R.Bevington, D.R.Robinson Data Reduction and Error Analysis for the Physical Science, WCB/McGraw-Hill (1992) Second Edition

[61] R.D.Field and R.P.Feynman Phys.Rev.D 15, 2590 (1977)

[62] E.Schnedermann et al Phys.Rev.C 48, 2462 (1993)

[63] R.E.Ansorge et al (UA5 Collaboration) Phys.Lett.B 199, 311 (1987)

[64] M.Heinz 2005 *Ph.D Thesis* University of Bern

[65] B.Norman 2003 *Ph.D Thesis* Kent State University

[66] S.Adler et al, (PHENIX Collaboration) Phys.Rev.Lett. 91 172301 (2003)

[67] J.W.Cronin et al, Production of hadrons at large transverse momenta at 200, 300, and 400 GeV Phys.Rev.D 11(1975)

[68] D.Antreasyan et al, Phys.Rev.D 19, 764 (1979)

[69] P.B.Straub et al, Phys.Rev.Lett. 68, 452 (1992)

[70] A.Krzywicki et al, Phys.Lett 85B, 407 (1979)

[71] A.Airapetian et al, (HERMES Collaboration) Phys.Lett.B 577, 37 (2003)

[72] X.N.Wang Phys.Rev.C 61, 064910 (2000)

[73] Y.Zhang et al, Phys.Rev.C 65, 034903 (2002)

[74] B.Z.Kopeliovich et al, Phys.Rev.Lett. 88, 232303 (2002)

[75] A.Accardi and D.Treleani, Phys.Rev.D 64,116004 (2001)

[76] I.Vitev and M.Gyulassy, Phys.Rev.Lett. 89, 252301 (2002)

[77] R.Hwa et al, Phys.Rev.C 70, 037901 (2004)

[78] D.M.Alde et al, (772 Collaboration) Nuclear Dependence of Dimuon Production at 800 GeV Phys.Rev.Lett. 64 24799(1990)

[79] J.-B.Blaizot *Preprint* hep-ph/0405305

[80] V.Topor-Pop et al *Preprint* nucl-th/0407095

[81] T.Hirano and Y.Nara *Preprint* nucl-th/0307015

[82] H.Caines (STAR Collaboration) J.Phys.G 31:S1057 (2005)

[83] J.Adams et al (STAR Collaboration) *Preprint* nucl-ex/0406003

[84] OPAL Collaboaration *Preprint* hep-ex/9808031

[85] SLD Collaboaration *Proceedings* SLAC-PUB-8160

[86] T.Sjostrand Comp.Phys.Comm. 1994 **82** 74

[87] G.Marchesini et al Comp.Phys.Comm. 1992 **67** 465

[88] K.J.Eskola et al Nucl.Phys. B323, 37 (1989)
D.Miśkowiec http://www-linux.gsi.de/ misko/overlap/

[89] A.Tang *PhD Thesis* Kent State University (2002)